Title

Single-nuclei transcriptome analysis of Huntington disease iPSC and mouse astrocytes implicates maturation and functional deficits

Journal

iScience, 26(1)

ISSN

2589-0042

Authors

Reyes-Ortiz, Andrea M

Abud, Edsel M

Burns, Mara S

et al.

Publication Date

2023

DOI

10.1016/j.isci.2022.105732

Peer reviewed

iScience

CellPress
OPEN ACCESS

Article

Single-nuclei transcriptome analysis of Huntington disease iPSC and mouse astrocytes implicates maturation and functional deficits

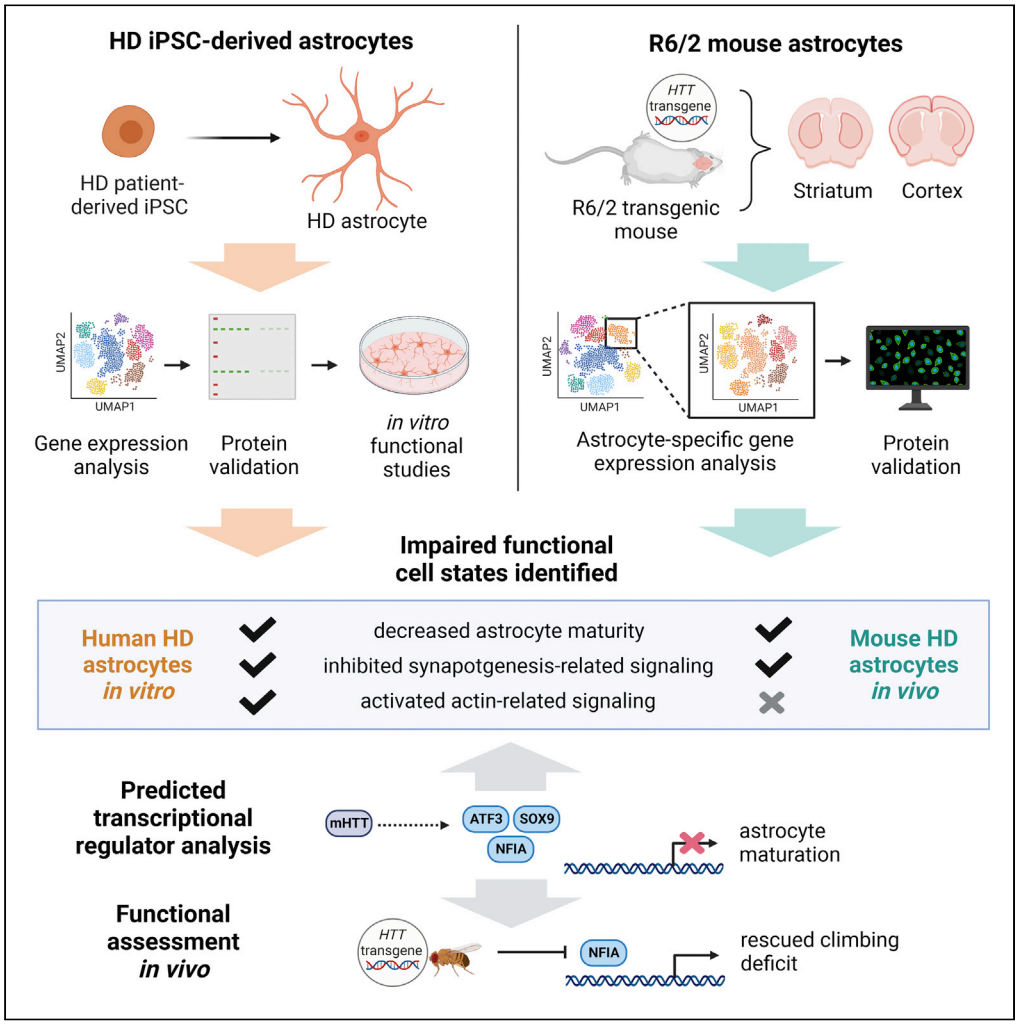

Andrea M. Reyes-Ortiz, Edsel M. Abud, Mara S. Burns, ..., Wayne W. Poon, Ryan G. Lim, Leslie M. Thompson

lmthomps@uci.edu

Highlights

Dysregulated HD astrocyte cell states may induce dysfunctional astrocyte properties

HD human and mouse astrocytes show altered maturation and glutamate signaling

HD iPSC-derived astrocytes show upregulated actin-mediated signaling

Astrogliogenesis transcription factors may drive HD astrocyte maturation deficits

Reyes-Ortiz et al., iScience 26, 105732
January 20, 2023
https://doi.org/10.1016/j.isci.2022.105732

iScience

CellPress
OPEN ACCESS

Article

Single-nuclei transcriptome analysis of Huntington disease iPSC and mouse astrocytes implicates maturation and functional deficits

Andrea M. Reyes-Ortiz,[1] Edsel M. Abud,[2,8] Mara S. Burns,[2,8] Jie Wu,[1] Sarah J. Hernandez,[2] Nicolette McClure,[3] Keona Q. Wang,[2] Corey J. Schulz,[3] Ricardo Miramontes,[5] Alice Lau,[4] Neethu Michael,[2] Emily Miyoshi,[2] David Van Vactor,[6] John C. Reidling,[5] Mathew Blurton-Jones,[2,3,5] Vivek Swarup,[2,5] Wayne W. Poon,[5] Ryan G. Lim,[5,7] and Leslie M. Thompson[1,2,3,4,5,7,9,*]

SUMMARY

Huntington disease (HD) is a neurodegenerative disorder caused by expanded CAG repeats in the huntingtin gene that alters cellular homeostasis, particularly in the striatum and cortex. Astrocyte signaling that establishes and maintains neuronal functions are often altered under pathological conditions. We performed single-nuclei RNA-sequencing on human HD patient-induced pluripotent stem cell (iPSC)-derived astrocytes and on striatal and cortical tissue from R6/2 HD mice to investigate high-resolution HD astrocyte cell state transitions. We observed altered maturation and glutamate signaling in HD human and mouse astrocytes. Human HD astrocytes also showed upregulated actin-mediated signaling, suggesting that some states may be cell-autonomous and human specific. In both species, astrogliogenesis transcription factors may drive HD astrocyte maturation deficits, which are supported by rescued climbing deficits in HD drosophila with NFIA knockdown. Thus, dysregulated HD astrocyte states may induce dysfunctional astrocytic properties, in part due to maturation deficits influenced by astrogliogenesis transcription factor dysregulation.

INTRODUCTION

Huntington disease (HD) is a devastating, autosomal-dominant neurodegenerative disease characterized by movement abnormalities, psychiatric disturbances, and cognitive impairment with no disease-modifying treatment. The genetic cause of HD is a CAG repeat expansion in the first exon of the *huntingtin* (*HTT*) gene, which encodes an expansion of a polyglutamine (polyQ) repeat tract in the huntingtin (HTT) protein.[1] When the *HTT* CAG repeat is expanded to 40 CAGs or above, HD is fully penetrant.[2,3] HTT is ubiquitously expressed in all cell types in the body and a broad range of cellular processes, predominantly in the brain, are impacted by chronic mutant HTT (mHTT) expression.[4,5] The mutation alters HTT structure and function, causing toxic gain of function and loss of normal HTT functions.[4] While the most overt HD neuropathology involves striatal neuronal loss and cortical atrophy, modeling of human-induced pluripotent stem cells (iPSCs) has been leveraged to identify HD cell-autonomous defects in non-neuronal cell types, such as endothelial cells that comprise the blood–brain barrier,[6] oligodendrocytes,[7] and astrocytes,[7–10] indicating that chronic expression of mHTT may induce intrinsic deficits within each cell type.

Astrocytes are the major glial cell type in the CNS, playing a critical role in regulating brain homeostasis. Astrocytes provide neurotrophic support through glutamate uptake and recycling, and contribute to synaptogenesis, neuronal maturation, and neuronal maintenance. Inter-astrocytic communication of calcium signaling is a function of astrocytes thought to help control blood flow for coupling to neuronal energy demand.[11,12] In addition to regulating a microenvironment that facilitates neuronal signaling, astrocytes maintain direct interactions with the brain endothelium to establish and maintain BBB and neuronal functions through soluble and physical communications.[13]

There has been growing literature characterizing the development and regulation of unique cellular states that define functional states of astrocytes. Moreover, impairments in these astrocyte states may generate

[1]Department of Biological Chemistry, University of California, Irvine, Irvine, CA 92617, USA

[2]Department of Neurobiology & Behavior, University of California, Irvine, Irvine, CA 92617, USA

[3]Sue and Bill Gross Stem Cell Research Center, University of California, Irvine, Irvine, CA 92617, USA

[4]Department of Psychiatry & Human Behavior, University of California, Irvine, Irvine, CA 92617, USA

[5]Institute for Memory Impairments and Neurological Disorders, University of California, Irvine, Irvine, CA 92617, USA

[6]Harvard Medical School, Department of Cell Biology, Boston, MA 02115, USA

[7]Senior author

[8]These authors contributed equally

[9]Lead contact

*Correspondence: lmthomps@uci.edu

https://doi.org/10.1016/j.isci.2022.105732

toxic functions that contribute to neurological disorders; however, the extent and mechanisms driving these impairments are just emerging for HD. HD astrocyte dysfunction appears to contribute to neuronal dyshomeostasis,[14–16] including impaired glutamate signaling and K+ buffering in astrocytes from HD mice.[15,17–19] Glutamate-related gene expression changes and dysfunction have recently been demonstrated in human patient postmortem tissue[19] and human patient iPSC-derived cells,[9] respectively. HD iPSC-derived astrocytes carrying juvenile-onset range CAG repeat lengths (77 CAG and 109 CAG) provided less support for functional neuronal maturation and contributed to glutamate-induced toxicity in iPSC-derived striatal neurons.[9] Other HD iPSC astrocyte studies revealed an increased autophagic response[8] and increased evoked inflammatory responses.[20] Additionally, purification of striatal astrocytes revealed common changes to RNA expression from R6/2 and Q175 HD mouse models, including core genes in calcium-dependent processes, G protein-coupled receptors, and glutamate receptor signaling[19] or in pathways regulating cytoskeletal formation and cell branching.[10] R6/2 uniquely showed changes to cholesterol regulation.[10] However, studies have yet to examine the molecular heterogeneity at a single-cell level to define distinct astrocyte states from striatum and cortex in HD mouse models and compare these to patient iPSC-derived astrocytes, as well as define potential mechanisms controlling their dysregulation.

With the development of single-cell and single-nuclei RNA-sequencing (sc- or snRNA-seq), astrocyte cell state transitions can now be compared at high resolution across multiple species, brain regions, and ages. A recent snRNA-seq study on HD astrocytes from postmortem patient cortical tissue identified heterogeneous cell states in HD human astrocytes.[21] Increased expression of metallothionein and heat shock genes and loss of astrocyte-specific gene expression was demonstrated. To further investigate HD human astrocyte cell states, human patient iPSC-derived astrocytes allow the ability to ascertain earlier, cell-autonomous events at the single-cell level that may lead to later changes in postmortem human tissue. Furthermore, iPSC-derived astrocytes allow for functional assessment, linking transcriptional states to astrocyte dysfunction. Findings from this model system can be compared to *in vivo* mouse and other HD model systems to evaluate common and novel HD phenotypes.

The goals of the present study are to further characterize astrocyte cell states in unaffected and HD contexts, identify drivers of transcriptional dysregulation, and to compare these states across human iPSC and mouse model systems. We investigated which astrocyte states exist in HD and if their transcriptional signatures can help predict altered astrocyte functions. We used unbiased snRNA-seq clustering followed by pathway enrichment and systematically compared signaling states between human and mouse astrocytes. Using this approach, we found altered astrocyte cell states related to glutamate signaling and maturation common to both HD iPSC-derived astrocytes (iAstros) and R6/2 astrocytes from the striatum and cortex compared to unaffected control astrocytes. We also identified disease cell states that predict activated extracellular matrix (ECM) and dysregulated actin cytoskeletal dynamics to be unique to human HD astrocytes, informing cell-autonomous dysregulation related to endogenous CAG repeat expansion in astrocytes. These transcriptional signatures were then used to identify regulatory genes that may be driving these alterations and could represent therapeutic targets. Overall, HD transcriptional changes reveal potential astrocyte maturation deficits and implicate that astrogliogenesis transcription factors, including ATF3 and NFIA, play a regulatory role contributing to HD pathogenesis. Together, these data provide a scientific resource of astrocyte cell states and transitions in both iPSC and mouse models of HD that may be useful for broadening understanding of the diverse astrocytes in the brain and guide therapeutic intervention in HD. The results suggest that loss of identity and maturation impairments are driven by altered expression of specific astrogliogenesis transcription factors.

RESULTS

HD iAstros exhibit altered morphology and astrocyte marker expression

To understand how CAG repeat expansion may influence astrocyte function in HD, we evaluated heterogenous astrocyte cell states through quantifiable gene expression analysis at the single-cell level. We first investigated whether altered cell state changes are reflected through cell-intrinsic mechanisms in astrocytes differentiated from human HD versus control iPSCs that express *mHTT* in an endogenous context. To do so, HD (46Q, 53Q) and control (18Q and 33Q)[6,23,24] iPSCs were differentiated into astrocytes (iAstros) (Table S1). Briefly, iPSCs were subject to prolonged neural induction to generate gliogenic neural stem cells followed by exposure to astrogliogenic factors for 60 days to induce morphologically and functionally mature astrocytes (Figures 1A, S1, and Table S2). HD iAstros had fewer astrocytic processes and had

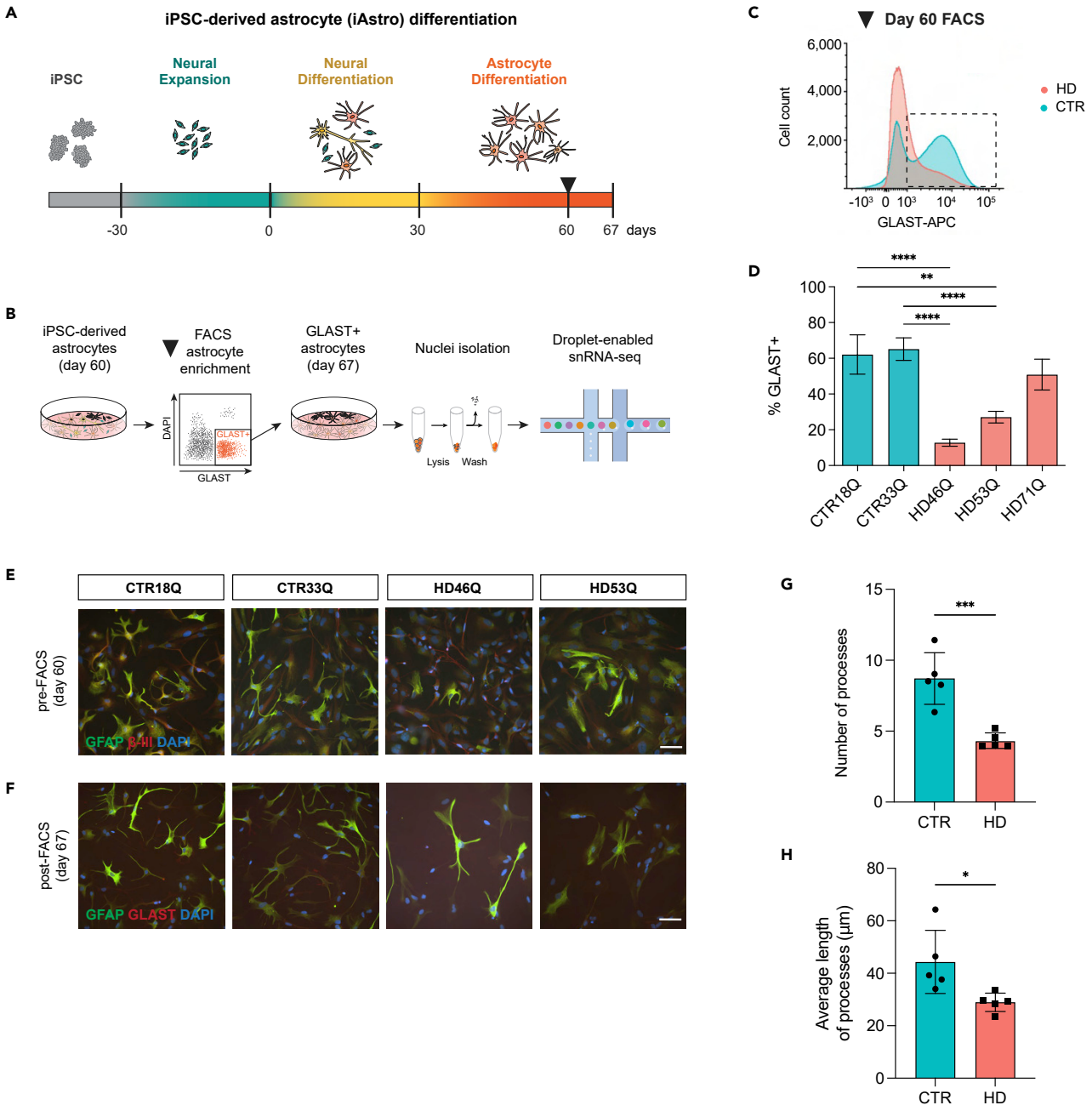

Figure 1. HD induced pluripotent stem cell-derived astrocyte derivation

(A) Astrocyte differentiation first begins with the differentiation of iPSCs into gliogenic neural stem cells, followed by 30 days of neural differentiation and 30 days of astrocyte maturation.

(B) At day 60, GLAST+/DAPI- fluorescence-activated cell sorting (FACS) was performed for astrocyte enrichment and astrocytes are subsequently matured for 7 days. At day 67, GLAST + astrocytes underwent single-nuclei isolation prior to droplet-enabled single-nuclei RNA-sequencing (snRNA-seq).

(C) Representative FACS histogram of HD and control iAstros GLAST expression level demonstrates HD astrocytes have decreased expression of GLAST at day 60.

(D) FACS quantification of GLAST+/DAPI- populations in day 60 iPSC-derived astrocytes (one-way ANOVA: 18Qv46Q ****$p < 0.0001$ [n = 8,11], 18Qv53Q **$p = 0.0028$ [n = 8,11], 33Qv46Q ****$p < 0.0001$ [n = 8,11], 33Qv53Q ****$p < 0.0001$ [n = 8,11], 18Qv71Q ns [n = 8,8], 33Qv71Q ns [n = 8,8]; n refers to biological [differentiation] replicates per line).

(E) Immunocytochemistry for GFAP, β-III tubulin (β-III), and DAPI at day 60 prior to FACS. Scale bar represents 100 µm.

(F) Immunocytochemistry for GFAP, SLC1A3, and DAPI 7 days post-FACS astrocyte enrichment. Scale bar represents 100 µm.

(G and H) HD iAstros have a significantly less total number of processes (unpaired t-test: CTRvHD ***$p = 0.0009$, n = 2–3 biological [differentiation] replicates per line, 25–30 images per line, 2 lines per genotype) (G) and significantly shorter average length of processes (unpaired t-test: CTRvHD *$p = 0.0253$, n = 2–3 biological [differentiation] replicates per line, 25–30 images per line, 2 lines per genotype) (H). All error bars indicate mean ± standard error mean. See also Figures S1–S3.

significantly larger cell volumes (Figure S2), indicating a potential deficit in astrocyte maturation.[25] We observed a significant decrease in the percentage of HD iAstros compared to control astrocytes that express GLAST, a functional glutamate transporter that clears the excitatory neurotransmitter from the extracellular space at synapses and is expressed by mature human astrocytes (Figures 1C and 1D). To directly compare a more pure population of HD to control mature astrocytes, GLAST-positive iAstros were isolated by fluorescence-activated cell sorting (FACS) and used for all subsequent studies (Figures 1B–1D and S3). GLAST-sorted HD and control cells express canonical astrocyte markers, like GFAP, and exhibit a classical star-like morphology (Figure 1F).

To further investigate morphological differences, we performed Sholl analysis on GLAST-sorted HD and control iAstros. HD GLAST-positive iAstros had less total number of astrocytic processes (Figure 1G) compared to GLAST-positive control iAstros. Additionally, HD GLAST-positive iAstros had shorter average length of processes (Figure 1H). Together, decreased length and number of astrocytic processes indicate that GLAST-positive HD astrocytes may have a decreased maturation profile compared to GLAST-positive control astrocytes.

Astrocyte transcriptional states in HD patient-derived iAstros reveals immature cell states regulated by aberrant astrogliogenesis transcription

Next, to investigate astrocyte transcriptional signatures in GLAST-sorted HD and control iAstros, we used snRNA-seq (Figure 1B). Among the 36,128 nuclei sequenced, nine distinct cell clusters were identified across HD and control iAstros representing unique astrocyte cell states across Uniform Manifold Approximation and Projection (UMAP) plots (Figures 2A and S4). HD or control clusters were identified by the number of iAstros per genotype by cluster (Figure 2B). Cluster 0 highly expressed mature astrocyte markers (Figure 2C) and represented a large proportion of control iAstros. Clusters 4 and 6 highly expressed other astrocyte markers, like *S100β* and *CD44*; these clusters were largely composed of control iAstros, with cluster 4 being primarily composed of a single control iAstro cell line (CTR33Q) (Figure S4). Clusters with a larger proportion of HD iAstros (e.g. clusters 1, 2, 3, 5, and 8) expressed low levels of mature astrocyte markers and/or high levels of immature human astrocyte markers (*MKI67 and TOP2A*), as transcriptionally defined from fetal human astrocytes.[25] In addition to expression of immature astrocyte markers, cluster 8 had high expression of progenitor markers, like *PAX6*, and had a larger population of HD cells. Cluster 7 also highly expressed immature astrocyte markers but showed similar proportions by genotype. Based on gene expression profiling of astrocyte developmental markers, control and HD iAstros reflect most cell states including various developmental states; however, HD iAstros show clear shifts in composition and full depletion of one of the control states, suggesting altered astrocyte maturation.

To molecularly assess the unique transcriptional signatures across iAstro clusters, the top markers per cluster were plotted and classified into gene categories (Figure 2D). iAstro clusters 0 and 6 had a large proportion of control iAstros and had the highest expression of neural support-related markers, like astrocyte-secreted synaptogenesis regulator *SPARCL1* and brain-derived neurotrophic factor receptor *NTRK2*. Immune-related genes, including *CD74* and many HLAs, were also highly expressed in iAstro cluster 6. Cluster 4 was composed of almost entirely control iAstros and represented a unique cell state with the most highly expressed genes related to long non-coding RNAs, like *NEAT1*, and reduced expression of ECM and progenitor markers. Clusters 1 and 2 contained a majority of HD iAstros and had high expression of adhesion-related molecules, *LGALS3* and *PALLD*, with cluster 2 also highly expressing calcium-binding molecules, *ANXA2* and *SLC3A1*. Immature astrocyte markers and cell cycle-related genes were highly expressed among a cluster with a large proportion of HD iAstros (cluster 3). Cluster 5 contained the largest proportion of HD iAstros and showed increased expression of several ECM-related genes, including collagens and fibronectin, along with calcium-binding and adhesion-related genes, which were also highly expressed in clusters 1 and 2 that contained a large proportion of HD iAstros. Cluster 8 was the smallest cluster (493 nuclei; 1.4% of total nuclei sequenced) and had a gene expression profile consistent with astroglial progenitors. Cluster 7 had equivalent proportions of HD and control iAstros and had a relatively high expression of DNA repair and transcription-related genes, like *FANCA* and *EZH2*. Overall, control states were enriched for astrocyte functions involved in neural support and neuroinflammation, while HD states were enriched for adhesion, ECM, and immature markers. These data highlight a loss of normal astrocyte functional support, potential developmental impairments, and ECM and adhesion-related alterations in HD iAstros. Finally, there is complete loss of a cell state in HD iAstros that showed high expression of *NEAT1*, a lncRNA regulator of transcription that has previously been implicated in HD[26,27] and is involved in altered neural cellular development and neural cell damage.[28,29]

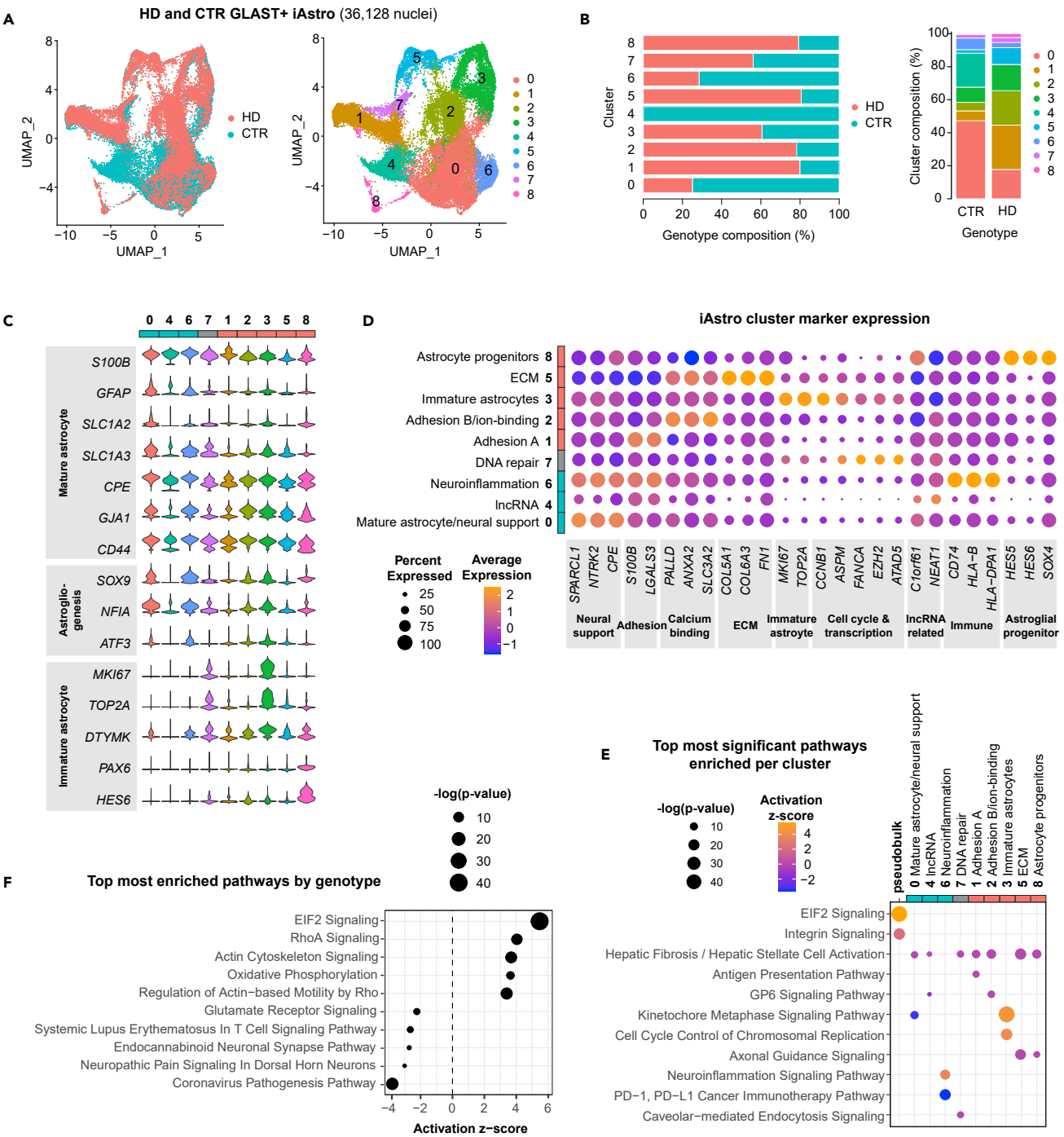

Figure 2. Dysregulated HD patient-derived astrocytes implicate immature cell states regulated by aberrant astrogliogenesis transcription

(A) GLAST + iAstro snRNA-seq UMAP by genotype (CTR n = 2, HD n = 2) and by cluster.

(B) Genotype composition of cells across astrocyte clusters and by genotype.

(C) Astrocyte marker genes across each iAstro cluster shows a decrease in maturation gene expression in several subclusters with larger proportion of HD cells (teal defined by >60% of the cluster were CTR cells, pink defined by >60% of cluster were HD cells, gray genotype represents 40–60% CTR or HD cells).

(D) Top cluster markers for each cluster for cell state classification.

(E) Top most significant pathways across all iAstro clusters used to classify cell state signatures. Psuedobulk genotype pathway enrichment using DEGs from all HD iAstros compared to control iAstros (Data S1) is included for comparison.

(F) Top 5 most activated and inhibited significant pathways in HD iAstros generated using genotype DEGs (Data S1). See also Figures S4 and S7.

To further explore the functional relevance of the iAstro clusters to biological pathways, ingenuity pathway analysis (IPA) pathway enrichment was performed on the genes differentially expressed between clusters. The top 2 most significant pathways per cluster were compared to assess the transcriptional signatures unique to each iAstro cluster and to differentially expressed genes (DEGs) by genotype (pseudobulk) (Figure 2E and Data S1). Hepatic fibrosis/hepatic stellate cell activation was a pathway among the top two significantly enriched pathways in all iAstro clusters except 3 and 6. Cluster 0, which had the largest proportion of control iAstros, exhibited significant inhibition of kinetochore metaphase signaling ($z = -3.16$, $p < 3e\text{-}9$), composed of cyclin, centromere, and histone-related molecules (*CCNB1*, *CDK1*, *CENPE*, *CENPK*, *H2AX*, and *H2AZ1*). Kinetochore metaphase signaling was instead activated in the immature cluster 3 ($z = 4.64$, $p < 2e\text{-}43$), that had a larger number of HD iAstros. The significant enrichment of hepatic fibrosis/hepatic stellate cell activation ($z = 0$, $p < 1e\text{-}5$) largely due to the downregulation of several collagens (*COL1A1*, *COL4A1*, and *COL4A2*) was present in cluster 4 that contained nearly all control iAstros. Another cluster that had a large proportion of control iAstros (cluster 6) had significant activation of neuroinflammatory signaling molecules ($z = 3.74$, $p < 6e\text{-}14$), like HLA transcripts and *SLC1A2*. The cluster with the second largest proportion of HD iAstros (cluster 1) had significant enrichment of antigen presentation pathway ($z = 0$, $p < 3e\text{-}7$) due to the expression of RNA transcripts that encode various HLA proteins (*HLA-A*, *HLA-C*, *HLA-DPA1*, *HLA-DRB5*, and *HLA-E*). The significant upregulation of several collagen transcripts (*COL11A1*, *COL18A1*, *COL1A2*, *COL27A1*, *COL3A1*, *COL4A1*, *COL4A2*, and *COL6A2*) caused a cluster with a large HD population (cluster 2) to be enriched in GP6 signaling molecules ($z = 0$, $p < 7e\text{-}8$). Cluster 3 contained a population that shifted toward mostly HD iAstros and had a significant activation of mitosis-related pathways, like kinetochore metaphase signaling pathway ($z = 4.65$, $p < 2e\text{-}43$) and cell cycle control of chromosomal regulation ($z = 4$, $p < 4e\text{-}19$) with the upregulation of cyclin-related genes, like *CDK1*, that suggest a mitotic activation of HD iAstros. The dysregulation of integrins (*ITGA11*, *ITGA6*, *ITGB1*, *ITGB4*, and *ITGB8*) and tubulins (*TUBA1A*, *TUBA1C*, *TUBB2A*, *TUBB2B*, and *TUBB6*) induced enrichment of axonal guidance signaling in cluster 5 ($z = 0$, $p < 3e\text{-}16$) and 8 ($z = 0$, $p < 1e\text{-}6$), which was comprised of 81% HD iAstros. Caveolar-mediated endocytosis signaling was significantly enriched ($z = 0$, $p < 4e7$) in cluster 7, which highly expressed integrin beta subunits. These nine iAstro clusters comprise unique transcriptional human astrocytic signatures that provide a glimpse into functionally relevant states of homeostatic and HD astrocytes.

To directly investigate genotype differences between HD and control iAstros, the top 5 significantly activated and top 5 significantly inhibited pathways by genotype (using genotype DEGs; Data S1) were plotted by activation score (Figure 2F). Eukaryotic initiation factor 2 signaling ($z = 5.47$, $p < 6e\text{-}41$) and actin signaling pathways ($z = 3.68$, $p < 6e\text{-}14$) were the most significantly activated pathways in HD iAstros, which contained overlapping actin-related genes (*ACTA2*, *ACTB*, *ACTC1*, and *ACTG2*). Glutamate receptor ($z = -2.24$, $p < 0.001$), endocannabinoid neuronal synapse ($z = -2.71$, $p < 0.04$), and neuropathic pain ($z = -3$, $p < 0.05$) signaling pathways were among the inhibited pathways in HD iAstros and contained genes encoding multiple glutamate receptors, *GRIA1-2* and *GRIN2A-B*. Additional inflammatory-related signaling pathways were among the most significantly inhibited, including systemic lupus erythematosus in T cell signaling ($z = -2.65$, $p < 0.002$) and coronavirus pathogenesis pathways ($z = -3.78$, $p < 1e\text{-}15$), with dysregulation of transcripts in common encoding HLA proteins and ribosome subunits.

Together, HD iAstro gene expression changes by cluster and by genotype highlight an inhibited glutamate receptor signaling state and unique astrocyte cell states, such as actin cytoskeletal signaling activation and immature astrocytes, that may contribute to loss of neural support and altered morphology or motility.

Defining HD striatal and cortical mouse astrocyte cell states

Human HD iAstros show shifts in cell state compositions, including complete loss of a state seen in control iAstros (cluster 4), that represents mature astrocytes with decreased expression of ECM-related genes and increased expression of NEAT1. We noticed a shift in the composition of HD iAstros that indicated an abundance of immature and progenitor-like cells before and after GLAST-positive sorting; these differences may represent deficits in astrogliogenesis which may lead to the functional state changes seen above. We next compared if similar state changes occur in an *in vivo* animal model of HD, and whether species-specific states exist. To assess the transcriptional cell states of striatal and cortical mouse astrocytes within a well-established system that recapitulates many transcriptome changes in human HD tissue,[30] we carried out snRNA-seq analysis of striatal and cortical brain regions from the rapidly progressing R6/2 HD model,

generated through the transgenic overexpression of the first exon of human HTT, and non-transgenic (NT) mice at ages 8 weeks (symptomatic) and 12 weeks (highly symptomatic)[31,32] (Figures 3A and 4A).

At the 12-week time point, we identified 13 and 16 distinct clusters from 26,509 striatal and 25,237 cortical nuclei sequenced, respectively. Expression of the *Slc1a2* astrocyte marker gene that encodes GLT1, a glutamate transporter that clears the excitatory neurotransmitter from the extracellular space at synapses, was used to identify the astrocyte cluster for each dataset (Figures 3B and 4B). The cluster with the highest *Slc1a2* expression was subset to investigate R6/2 astrocyte-specific dysregulation via sub-clustering and further transcriptomic analyses. Due to a small population of cells with relatively low levels of astrocyte markers and high expression of vascular markers *Pdgfrb* and *Flt1*,[33] additional sub-setting was necessary before sub-clustering the cortical astrocyte cluster (Figure S5). Upon sub-clustering all 12-week R6/2 astrocyte clusters, we identified six striatal astrocyte clusters and five cortical astrocyte clusters visualized using UMAP (Figures 3C and 4B). Interestingly, the total number of clusters identified was less than the human iAstros which may represent species differences, considering the known complexity of human glia versus mouse glia.[34] Diverse cellular states were represented across each mouse dataset and to identify genotype composition by cluster, the total number of cells per genotype was quantified by cluster. Striatal clusters 2 and 4 were significantly enriched in R6/2 compared to NT, while cortical cluster 0 was significantly enriched in R6/2, indicating these clusters are relatively novel to the R6/2 condition (Figures 3D and 4C). R6/2 striatal astrocytes had a larger number of differentially expressed genes by genotype compared to cortical astrocytes (Figures S6 and S7).

Expression of mature astrocyte marker genes and transcription factors regulating astrogliogenesis were visualized across astrocyte clusters (Figures 3E and 4D). R6/2-enriched striatal astrocyte clusters 2 and 4 as well as R6/2-enriched cortical cluster 0 had a lower expression of several classic astrocyte identity genes, such as *Slc1a2* and glutamate-ammonia ligase (*Glul*), compared to NT-enriched striatal cluster 1. Similarly, cortical astrocyte clusters 1 and 3 had a lower expression of these astrocyte identity genes compared to cluster 0. Decreased expression of astrocyte markers in R6/2-enriched clusters indicates that dysregulated cell states exist in R6/2 astrocytes and may reflect differences in astrocyte development or a loss of cell identity genes. Altogether, there was a shift in the R6/2 astrocytes toward more immature cell states.

Inhibited synaptogenesis-related signaling states in R6/2 striatal astrocytes

We next molecularly assessed the cell states identified in striatal and cortical R6/2 and NT mouse astrocytes. First, the top highly expressed gene markers per cluster were used to classify clusters into functionally relevant categories (Figures 3F and 4E). Several of the highest expressing genes in significantly NT-enriched striatal cluster 1 and cortical cluster 2 included astrocyte-enriched glutamate transporter (*Slc1a2) and* glutamate receptors *(Gria1*, *Gria2*, and *Grin2c)*, like iAstro clusters 0 and 6 that had larger proportion of control cells. The striatal clusters with the largest proportion of NT astrocytes (clusters 1 and 3) also had high expression of GABA transporter *Slc6a11* and GABA receptor *Gabbr2*. Cortical clusters 1 and 2 had a high expression of an actin-binding gene *Clmn* and a phagocytic receptor *Mertk*. Cortical cluster 4, which had a large proportion of NT astrocytes, exhibited high expression of neural regulatory genes (*Anks1b and Nrg3*), axonal/synaptic-related genes (*Robo2*, *Dlg2*, *and Lrtm4*), and *Kcnip4*, which encodes a potassium channel-interacting protein.

Among the striatal clusters with significantly more R6/2 cells compared to NT, striatal clusters 2 and 4 had the highest expression of developmental-related genes, RNA polymerase (*Polr2a*), and a nuclear receptor involved in neurogenesis (*Nr6a1*). R6/2-enriched striatal cluster 2 also had the highest expression of two ECM-related genes: glycoprotein-related *Sgcd* and cell adhesion molecule *Nrxn3*. R6/2-enriched cortical cluster 0 highly expressed *Ogt*, a glycosyltransferase regulator. Similar to iAstro clusters 1 and 2 that had large proportion of HD iAstros, striatal cluster 5 had the highest expression of sodium, potassium, or calcium ion-binding genes, like *Adgrv1*, *Nkain2*, and *Cacnb2*, except for the potassium channel, *Kcnd2*, which was most highly expressed in striatal clusters 1 and 2. Cortical cluster 3 exhibited high expression of calcium-binding genes, *Adgrv1* and *Cacnb2*, and was not enriched by genotype.

To further explore the potential functional relevance of these striatal astrocyte clusters, we ran pathway enrichment analysis (IPA) on the DEGs (Data S2) for each cluster compared to all other striatal (Figure 3G) and cortical astrocytes (Figure 4F). Striatal cluster 0 had the highest activation of an amyotrophic lateral sclerosis signaling pathway ($z = 1$, $p < 4e\text{-}6$) and glutamate receptor signaling ($z = 0.38$, $p < 1e\text{-}8$) due to

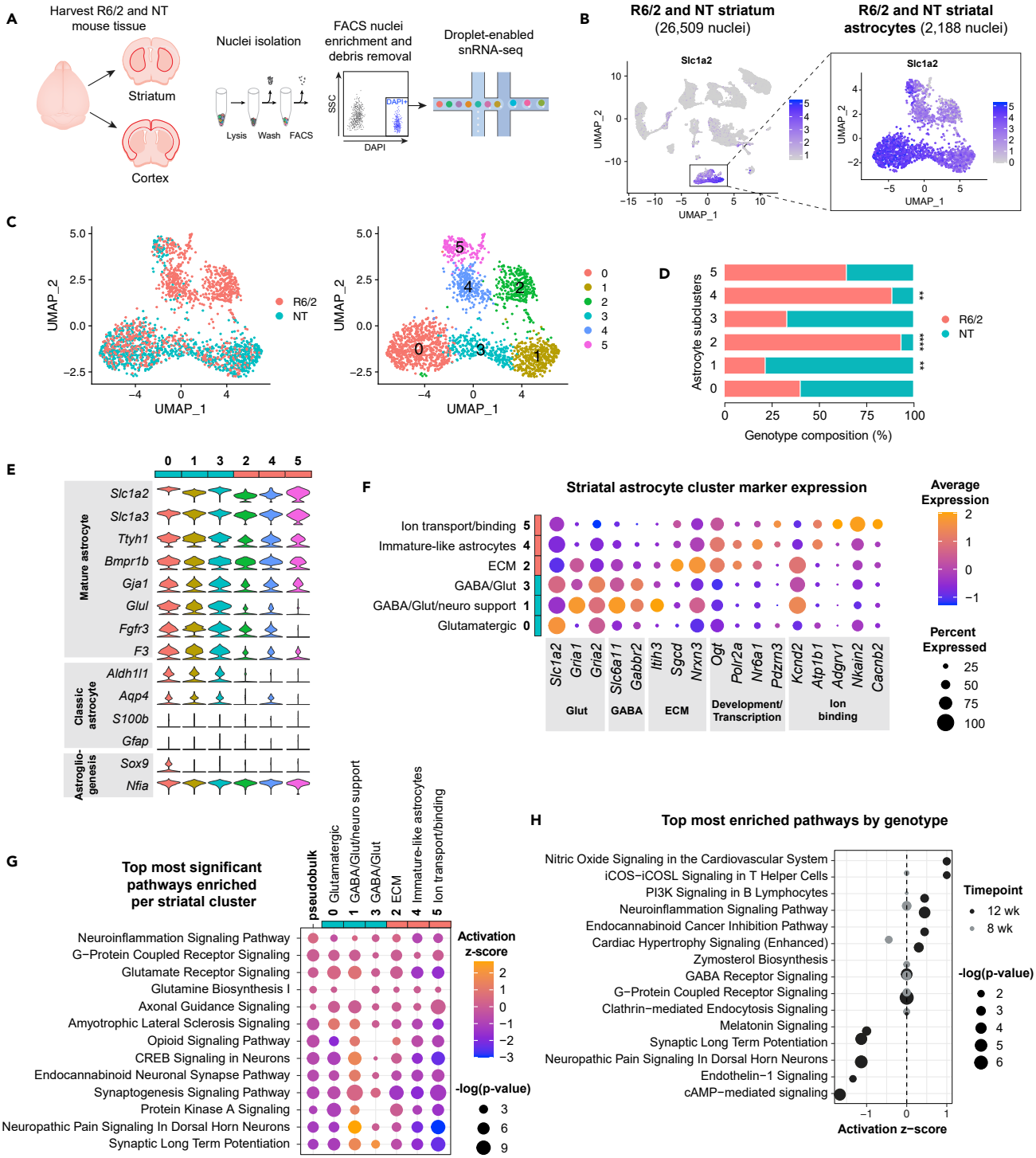

Figure 3. Striatal R6/2 astrocytes exhibit immature and decreased synaptogenesis cell states

(A) Experimental workflow for snRNA-seq analysis where striatal and cortical tissue was harvested from NT and R6/2 mice, dissociated, then underwent single-nuclei isolation and FACS separation prior to droplet-enabled snRNA-seq.

(B) UMAP of all 12-week striatal snRNA-seq libraries performed on aggregated peak matrix. The astrocyte cluster was identified by expression of *Slc1a2*.

(C) UMAP subset analysis of astrocyte cluster identified several astrocyte subclusters across R6/2 and NT.

(D) Genotype composition of cells across astrocyte subclusters (two-way ANOVA, Bonferroni multiple comparisons test performed on number of nuclei/ mouse within each subcluster adjusted p values: cluster 0 p = 0.0809, cluster 1 **p = 0.0012, cluster 2 ****p < 0.0001, cluster 3 p = 0.5160, cluster 4 **p = 0.0057, cluster 5 ns; n = 3 mice per genotype per timepoint).

Figure 3. *Continued*

(E) Astrocyte marker genes across each subcluster shows a decrease in maturation gene expression in several striatal subclusters with larger proportion of R6/2 cells (teal defined by >60% of the cluster were NT cells, pink defined by >60% of cluster were R6/2 cells).

(F) Top cluster markers for each cluster for cell state classification.

(G) Top most significant pathways across all striatal astrocyte clusters used to classify cell state signatures. Psuedobulk genotype pathway enrichment using DEGs from all 12-week R6/2 striatal astrocytes compared to all 12-week NT striatal astrocytes (Data S2) is included for comparison.

(H) Top most enriched significant pathways by age for 8- and 12-week (wk) striatal R6/2 astrocytes generated using genotype DEGs (Data S2). See also Figures S5 and S7.

the high expression of overlapping genes that encode proteins responsible for glutamate-glutamine cycling in astrocytes (*Slc1a2*, *Glul*, *Gria1*, *Grid1*, and *Grin2c)*. Striatal cluster 1 was significantly enriched in NT astrocytes and had the highest activation in neuropathic pain signaling ($z = 2.67$, $p < 3e\text{-}8$) and synaptic long-term potentiation ($z = 1.6$, $p < 7e\text{-}7$), due to the overlap in upregulated genes *Gria1*, *Gria2*, and *Grin2c*. Striatal cluster 3 had a large proportion of NT astrocytes and exhibited significant activation of synaptic long-term potentiation ($z = 2$, $p < 0.001$) and synaptogenesis signaling ($z = -1.35$, $p < 9e\text{-}10$), with upregulation of *Gria2* in both pathways. Cortical cluster 4 was also largely composed of NT astrocytes and had significant activation of synaptogenesis signaling ($z = 6.97$, $p < 7e\text{-}29$) and calcium signaling ($z = 6.08$, $p < 3e\text{-}13$) through upregulation of genes that encode calcium/calmodulin-dependent protein kinases (*Camk2a*, *Camk3b*, and *Camk4*) and calcium voltage-gated channel subunits (*Cacna1b*, *Cacna2d1*, and *Cacnb4*).

Cortical cluster 2, which was largely composed of NT astrocytes, and non-genotype-enriched cluster 1 were significantly enriched in glutamate receptor signaling due to expression of *Grin2c* and *Slc1a2*, with predicted activation in cluster 1 ($z = 1$, $p < 5e\text{-}8$) but no predicted activation for cluster 2 ($z = 0$, $p < 0.002$). Cortical cluster 1 also exhibited a predicted activation of synaptogenesis signaling ($z = 2.83$, $p < 0.0006$). Glutamate receptor signaling was the most significantly enriched pathway for cortical cluster 3, with a predicted inhibition ($z = -1.34$, $p < 4e\text{-}11$), like HD iAstros. Additionally, Rho GDP-dissociation inhibitor (RhoGDI) signaling was predicted to be most activated and synaptogenesis signaling was the most inhibited predicted pathway for non-genotype-enriched cortical cluster 3.

Among the striatal astrocyte clusters significantly enriched with R6/2 cells, the most significant pathways across striatal clusters 2 and 4 were synaptogenesis signaling (cluster 2: $z = -1.35$, $p < 9e\text{-}10$; cluster 4: $z = -1.81$, $p < 2e\text{-}7$) and glutamate receptor signaling (cluster 2: $z = 0$, $p < 3e\text{-}7$; cluster 4: $z = -1.34$, $p < 9e\text{-}7$) specifically due to the downregulation of genes associated with glutamate receptors, like *Gria1* and *Gria2*. Neuropathic pain ($z = -3$, $p < 1e\text{-}9$) was among the most inhibited pathways for striatal cluster 5, as well as synaptic long-term potentiation ($z = -2.36$, $p < 8e\text{-}10$) and cAMP response element-binding protein (CREB) signaling ($z = -2.36$, $p < 1e\text{-}8$). R6/2-enriched cortical cluster 0 was most significantly enriched in glutamate receptor signaling ($z = -1$, $p < 7e\text{-}9$), and synaptogenesis signaling pathway was predicted to be the most inhibited pathway ($z = -3.16$, $p < 2e\text{-}6$).

Overall, the data suggest a loss of glutamate signaling and synaptogenesis-related pathways across R6/2 astrocytes, and activation of ECM and immature-like astrocyte states, similar to human HD patient iAstros. These data highlight similarities with the human HD iAstros that suggest maturation impairments, with a particular focus on glutamate receptor and synaptogenesis-related dysregulation.

HD mouse astrocyte temporal and brain region comparisons

We next examined transcriptional changes that occur in R6/2 astrocytes with progressive disease. We assessed the activation scores of the top ten most significant pathways enriched in 8-week mouse astrocyte signaling states and 12-week mouse astrocyte signaling states compared to age-matched NT mouse striatal astrocytes (Figure 3H and Data S2). As expected, there was overlap of many relevant pathways between the 8- and 12-week striatal R6/2 astrocytes. The 12-week astrocytes exhibited increased predicted activation of iCOS-iCOSL signaling in T helper cells (12-week: $z = 1$, $p < 0.008$; 8-week: $z = 0$, $p < 0.032$), PI3K signaling in B lymphocytes (12-week: $z = 0.447$, $p < 0.003$; 8-week: $z = 0$, $p < 0.048$), and neuroinflammation signaling (12-week: $z = 0.447$, $p < 5e\text{-}5$; 8-week: $z = 0$, $p < 0.001$). *Chuk*, which encodes an inhibitor of the transcription factor NFκB complex, was an overlapping upregulated gene across the three inflammatory pathways. The most significantly inhibited pathway in 12-week striatal astrocytes was cAMP-mediated signaling ($z = -1.67$, $p < 3e\text{-}5$). Interestingly, cardiac hypertrophy signaling was the most significantly inhibited pathway predicted in the 8-week striatal R6/2 astrocytes

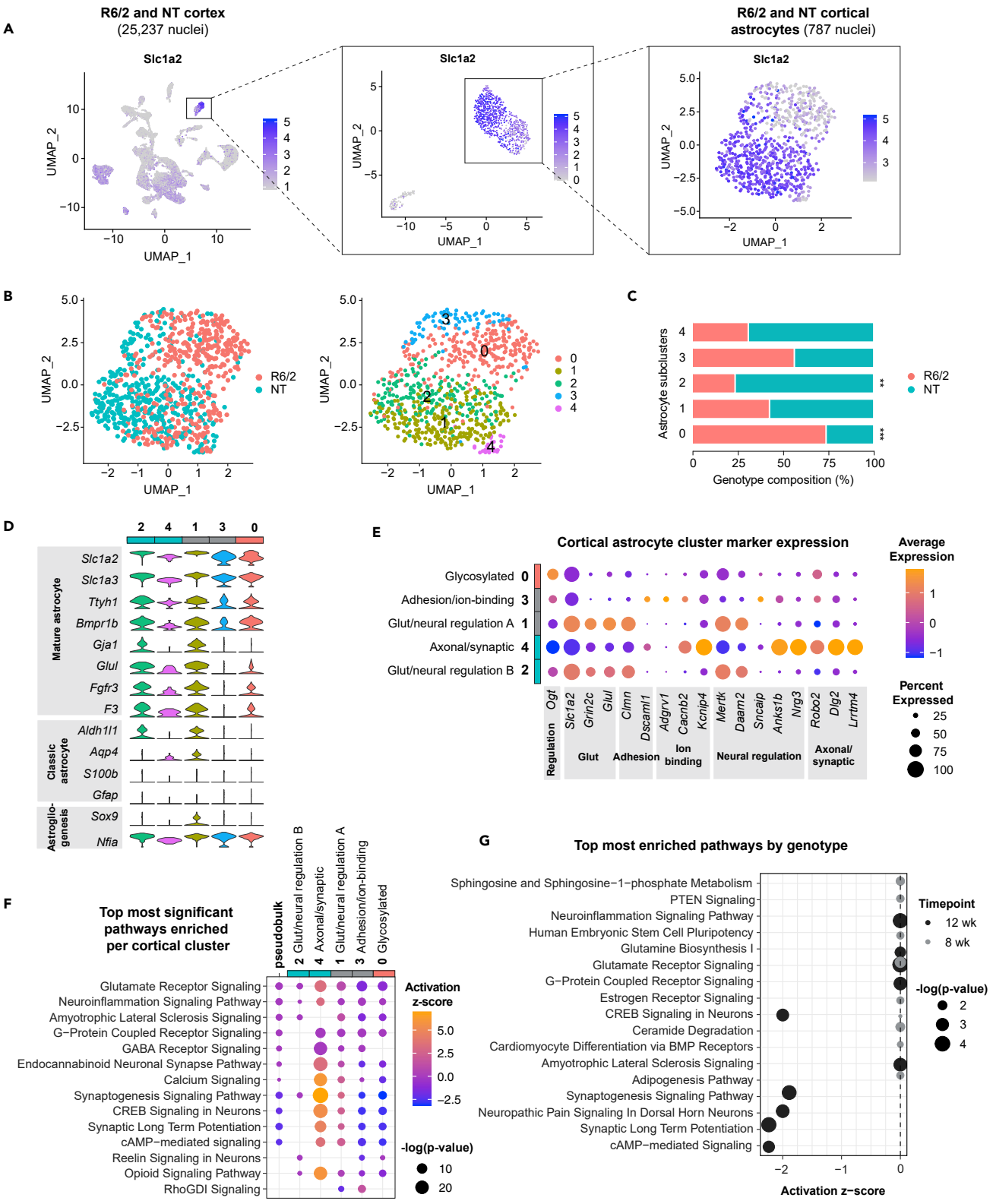

Figure 4. Cortical R6/2 astrocytes exhibit inhibited neuronal homeostatic signaling and decreased astrocyte marker expression

(A) UMAP of all 12-week cortical snRNA-seq libraries performed on aggregated peak matrix. The astrocyte cluster was identified by expression of astrocyte marker gene, *Slc1a2*. Additional subclustering was necessary to subset out cortical vascular cells from astrocytes.

Figure 4. *Continued*

(B) UMAP subset analysis of astrocyte cluster identified several astrocyte subclusters across R6/2 and NT.

(C) Genotype composition of cells across astrocyte subclusters (two-way ANOVA, Bonferroni multiple comparisons test performed on number of nuclei/mouse within each subcluster adjusted p values: cluster 0 ***p = 0.0004, cluster 1 ns, cluster 2 **p = 0.0064, cluster 3 ns, cluster 4 ns; n = 3 mice per genotype per time point).

(D) Astrocyte marker genes across each subcluster genotype bar depicting which clusters were composed of a larger proportion of R6/2 cells (teal defined by >60% of the cluster were NT cells, pink defined by >60% of cluster were R6/2 cells, gray genotype represents 40%–60% NT or R6/2 cells).

(E) Top cluster markers for each cluster for cell state classification.

(F) Top most significant pathways across all cortical astrocyte clusters used to classify cell state signatures. Psuedobulk genotype pathway enrichment using DEGs from all 12-week R6/2 cortical astrocytes compared to all 12-week NT cortical astrocytes (Data S2) is included for comparison.

(G) Top most enriched significant pathways by age for 8- and 12-week (wk) cortical R6/2 astrocytes. See also Figures S5 and S7.

($z = -0.447$, $p < 0.008$) due to expression of genes such as *Camk2g*, *Chuk*, and *Fgf14*, but was predicted to be activated in 12-week striatal R6/2 astrocytes ($z = 0.302$, $p < 6e\text{-}4$). In general, the most significantly enriched pathways in 8-week striatal astrocytes had no predicted activation or inhibition. By 12 weeks, R6/2 astrocytes had more severe predicted activation or inhibition of these overlapping pathways that correlates with increased severity in motor phenotypes,[35] suggesting increased astrocyte dysfunction with disease progression. The overlap in top pathways between 8 and 12 weeks with progressive dysregulation of similar genes, indicates that at these two symptomatic timepoints, R6/2 astrocytes are similarly dysregulated. Taken together, R6/2 astrocytes exhibited inhibition of neuronal homeostatic signaling pathways, suggesting how mHTT-expressing striatal astrocytes could contribute to neuronal dysregulation in R6/2 mice.

Temporal changes occurring in R6/2 cortical astrocytes were also evaluated (Figure 4G and Data S2). The most significantly enriched pathways in 12-week cortical astrocytes were predicted to be inhibited or had no activation scores. Among those were glutamate receptor signaling ($z = 0$, $p < 8e\text{-}5$), synaptic long-term potentiation ($z = -2.236$, $p < 2e\text{-}4$), and neuroinflammation signaling pathway ($z = 0$, $p < 2e\text{-}4$), with glutamate receptor *Grin2c* being a common downregulated gene across the three pathways. The most significantly enriched pathway in 8-week cortical astrocytes was glutamate receptor signaling ($z = 0$, $p < 0.004$), which was also significantly enriched in 12-week cortical astrocytes due to downregulation of related genes (*Glul*, *Gria2*, *Grin2c*, and *Slc1a2*). The 8-week cortical astrocyte pathways had no predicted activation or inhibition ($z = 0$), like 8-week striatal astrocytes. These findings further demonstrate dysregulated signaling in R6/2 astrocytes related to neuronal homeostasis, particularly glutamate receptor signaling (which overlaps with results from HD iAstros), increases in severity with disease progression—although diversity in cell states was less severe in R6/2 cortical astrocytes compared to R6/2 striatal astrocytes.

To determine the impact of mHTT on R6/2 astrocyte cell states by brain region, we directly compared striatal and cortical astrocyte pathway enrichment performed on genotype DEGs from both timepoints (Figures 5A, S5, and Data S2). R6/2 12-week striatal and cortical astrocytes showed significant inhibition of neural regulatory-related signaling, including synaptic long-term potentiation, synaptogenesis, and CREB signaling in neurons. The most significant pathways enriched in R6/2 8-week striatal and cortical astrocytes had low or no predicted activation scores, but the individual pathways were more unique to each brain region. When evaluating each region, striatal 8-week top pathways included neuroinflammation and GABA receptor signaling, while cortical 8-week top pathways were glutamate receptor signaling, ceramide degradation, and sphingosine-1-phosphate (S1P) metabolism; this highlights the unique cellular processes in metabolic regulation across these two brain regions during this stage in HD pathogenesis that may drive changes at later stages. There were many overlapping significant pathways relating to synaptogenesis signaling in 12-week striatal and cortical timepoints but had increased predicted inhibition in cortical astrocytes. These shared and unique pathways across astrocytes in age and brain region highlight the unique astrocyte cell states that may contribute to R6/2 pathogenesis across these two highly affected brain regions.

As the overlapping pathways across time points and brain regions suggested, there was significant astrocyte genotype DEG overlap (Figure 5B and Data S2). The set of 56 overlapping 12-week striatal and cortical DEGs were genes all dysregulated in the same direction and may represent common signatures in astrocytes independent of region (Figure 5C). Individual examination of each of these genes was performed to uncover commonalities contributing to transcriptional dysregulation in R6/2 mouse astrocytes at this severe disease stage. *Gria2* and *Grin2c* were present in a majority of the overlapping dysregulated signaling

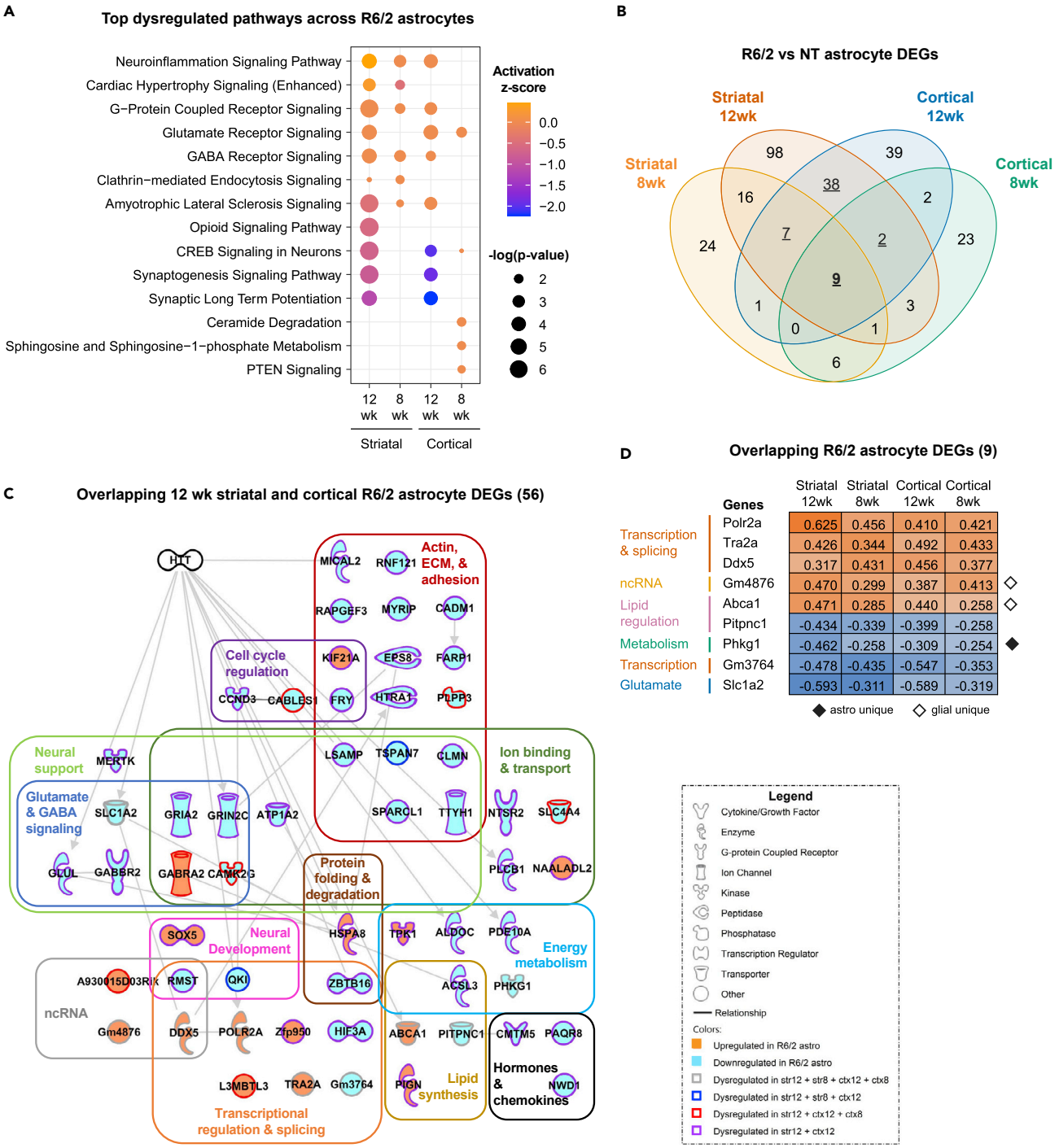

Figure 5. Shared R6/2 astrocyte dysregulation across brain regions and ages highlights neuronal homeostasis dysregulation

(A) Top most significant canonical pathways across brain regions and ages (12 week [12 wk] and 8 week [8 wk]).

(B) Venn diagrams of significant differentially expressed genes (DEGs) in R6/2 mouse astrocytes across timepoints and brain region (exact hypergeometric probability calculated using 56 DEG overlap for 12-week striatum [174 DEGs] vs 12-week cortex [98 DEGs] ****p < 8e-113, 33 DEG overlap for 12-week striatum [174] vs 8-week striatum [64 DEGs] ***p < 7e-64, 13 DEG overlap for 12-week cortex [98 DEGs] vs 8-week cortex [46 DEGs] *p < 8e-25, 16 DEG overlap for 8-week striatum [64 DEGs] vs 8-week cortex [46 DEGs] **p < 3e-35 using 46,206 as the number of genes with nucleotide sequence data in the mouse genome database). Underlined numbers represent the 56 DEGs overlapping between 12 week striatal and 12 week cortical astrocytes. The underlined and bolded 9 represents the 9 DEGs that overlap across all four R6/2 astrocyte datasets.

Figure 5. *Continued*

(C) Overlap of 12-week striatal and cortical astrocyte (56) DEGs highlight pathway dysregulation in R6/2 astrocytes across both brain regions in symptomatic mice.

(D) The nine overlapping DEGs across all datasets. Solid orange symbol represents upregulated DEG and solid cyan symbol represents downregulated DEG. Solid black diamond denotes a DEG unique to only astrocytes, while a white diamond denotes a DEG unique to astrocytes, oligodendrocytes, and oligodendrocyte progenitor cells. See also Figures S6 and S7, and Data S2.

pathways related to neuronal support, glutamate receptor signaling, and ion binding; this highlights how aberrant R6/2 astrocytes affect the regulation of neuronal homeostasis. There were also several genes related to both neural support and extracellular matrix/adhesion-related signaling, such as *Sparcl1*, *Ttyh1*, and *Tspan7*. Together, this dysregulated astrocyte signaling at 12 weeks may highlight two major dysfunctions occurring across R6/2 astrocytes and how it affects the cells they are meant to support, therefore contributing to pathogenesis.

To further assess the common dysregulation across R6/2 astrocytes, we examined the nine genotype DEGs that were common across astrocytes from both brain regions and time points. These genes all had very similar expression levels that often became more severe with age, with striatal 12-week astrocytes typically having the most extreme expression of these nine common DEGs (Figure 5D). Exceptions included several splicing and transcription-related genes (*Gm3764*, *Tra2a*, and *Ddx5*) that had the highest fold change in DEGs from cortical 12-week R6/2 astrocytes compared to cortical NT astrocytes. A non-coding RNA (*Gm4876*) and a lipid regulator (*Abca1*) were DEGs unique to only glial cell types (astrocytes, oligodendrocytes, and/or oligodendrocyte progenitor cells) in the larger R6/2 snRNA-seq dataset. Among these overlapping astrocyte DEGs, the downregulation of the glycogen phosphorylase activator, *Phkg1*, was unique to only astrocytes compared to other R6/2 cell types and highlights the potential dysregulation of glycogen breakdown in R6/2 astrocytes. These common DEGs may represent core processes, metabolic and transcriptional, that become dysregulated at an early stage of HD pathogenesis and give rise to other changes seen at 8 and 12 weeks in the R6/2 mice. The changes in these metabolic and transcriptional processes may lead to the altered signaling described above related to synaptogenesis, glutamate signaling, calcium signaling, and inflammation.

Inhibition of glutamate signaling in HD iAstros and R6/2 astrocytes

A significantly inhibited glutamate receptor signaling cell state was identified in R6/2 and HD iAstro clusters. The presence of these states in both the mouse and iPSC model suggests that this is a core feature of HD astrocytes and likely arises intrinsically from the expression of mHTT. Genes that encode glutamate transporters (*SLC1A2* and *SLC1A3*) and glutamate receptors (*GRIA1*, *GRIA2*, and *GRIN2A*) were significantly downregulated across both models of HD astrocytes (Figures 6A and 6B; Data S1 and S2). To confirm the intrinsic loss of glutamate signaling in HD astrocytes, we investigated protein levels of a representative glutamate receptor 1 (GluR1), encoded by *GRIA1*. Western blot analysis for GluR1 was performed on HD and control iAstros and showed significantly decreased GluR1 in HD iAstros compared to control iAstros (Figure 6C). Due to the common downregulation of glutamate-related signaling seen in both mouse and human HD astrocytes in this study and in previously published results,[50–52] we next assessed if our HD iAstros showed a functional impairment. HD iAstros demonstrated decreased functional uptake of glutamate when exogenous glutamate was added *in vitro* (Figure 6D). Since the downregulation of glutamate transporters and receptors was observed in both models, and we demonstrated decreased functional glutamate uptake in HD iAstros, we suspect that this is a cell-autonomously downregulated signaling pathway in HD astrocytes. The sorted iAstros are not exposed to signaling from neurons, and recapitulation of this alteration provides evidence for cell-autonomous effects. Inhibition of the uptake of glutamate can influence HD pathogenesis by contributing to glutamate neurotoxicity.

Activation of ECM and actin in HD iAstros

ECM and actin cytoskeletal signaling were processes uniquely activated in a subcluster of HD iAstros which were not identified in R6/2 astrocytes. While there were several actin, ECM, and adhesion-related DEGs (e.g. *CADM1*, *CLMN*, and *MICAL1*) present in overlapping 12-week striatal and cortical R6/2 astrocytes (Figure 5C), this did not trigger significant enrichment of specific actin or ECM signaling pathways, unlike HD iAstros. We investigated the genes contributing to ECM and actin cytoskeletal signaling activation in the HD and control iAstro cell lines to determine the genes controlling these dysregulated pathways (Figure 7A and Data S1). Genes related to extracellular signaling (*ITGB1* and *ITGA3*) and those regulating actin

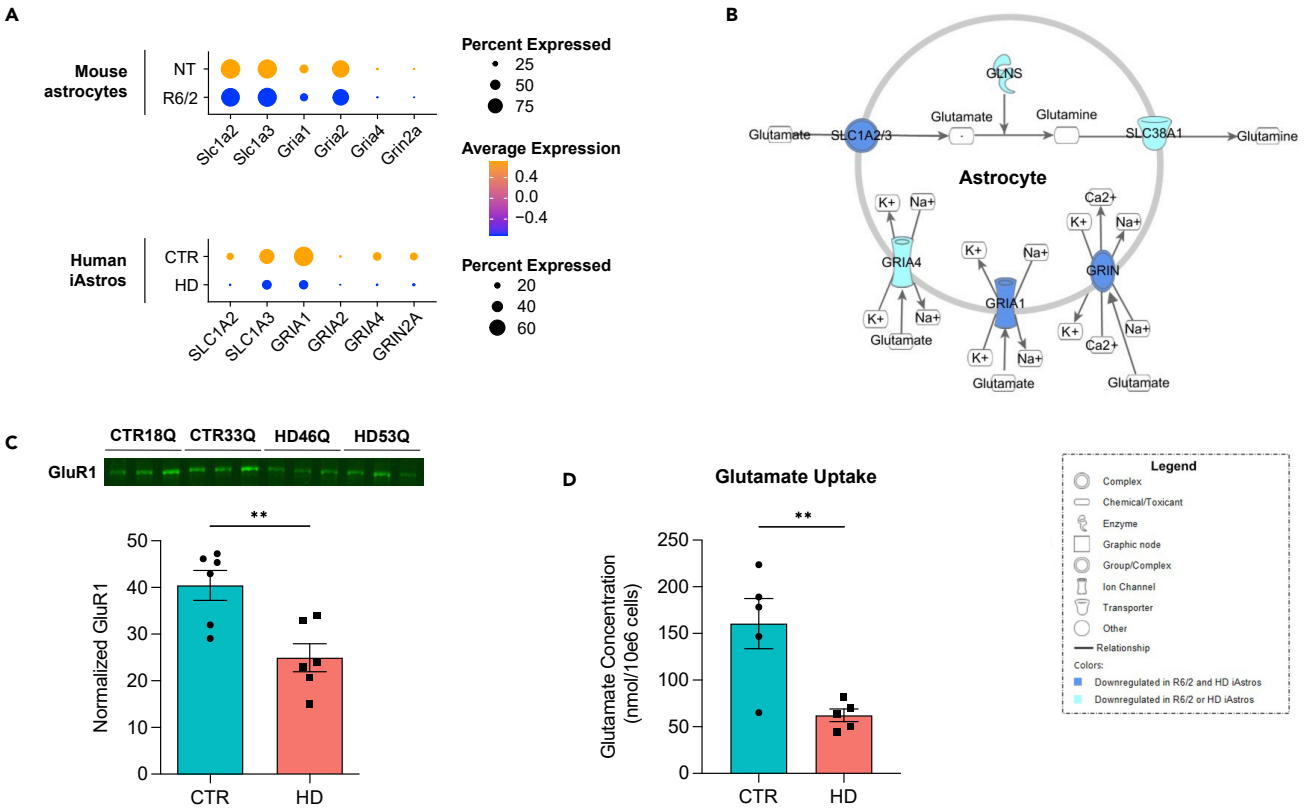

Figure 6. HD astrocyte inhibited glutamate receptor signaling in R6/2 and HD iAstros

(A) Significantly downregulated molecules in glutamate receptor signaling pathway across R6/2 and HD iAstros.

(B) Glutamate receptor signaling network R6/2 and HD iAstro snRNA-seq shows significant downregulation of glutamate-related molecules across multiple models of HD astrocytes. Solid blue symbol represents downregulated DEG in R6/2 and HD iAstros and solid cyan symbol represents downregulated DEG in R6/2 or HD iAstros.

(C) GluR1 Western blot and quantification demonstrates significant decreased GluR1 in HD iAstros (unpaired t-test: **p = 0.0054, n = 3 biological [differentiation] replicates per line, 2 lines per genotype).

(D) HD iAstros uptake significantly less glutamate than control (CTR) iAstros (unpaired t-test: **p = 0.0075, n = 2–3 biological [differentiation] replicates per line, 2 lines per genotype). All error bars indicate mean ± standard error mean. See also Data S1 and S2.

dynamics (*ACTN1*, *Talin*, and *ERM*), actin polymerization (*F-actin*, *PFN*, *and ARP2/3*), and overall cytoskeletal reorganization (*MYL and Myosin*) were all significantly upregulated in HD iAstros (Figure 7B and Data S1). Given the potential disruption of the actin cytoskeleton, we investigated whether filamentous actin (F-actin) protein expression was increased in our HD iAstros as a surrogate readout. Phalloidin in-cell westerns were performed on HD and control iAstros and showed that HD iAstros had significantly increased expression of F-actin compared to control iAstros (Figure 7C). Additionally, HD iAstros exhibited increased levels of the F-actin crosslinking protein, actinin (ACTN), compared to control iAstros (Figure 7D), suggesting increased actin cytoskeletal scaffolding as a gain of cell state in HD iAstros. Taken together, ECM and actin cytoskeletal signaling are cell-autonomous and potentially early-activated signaling pathways unique to patient-derived HD astrocytes that may contribute to morphological changes or increased adhesion in HD astrocytes.

Aberrant astrogliogenesis transcriptional regulators in HD astrocytes

To investigate the potential regulatory mechanisms controlling human HD astrocyte dysregulation, we used genotype DEGs in HD iAstros (Data S1) to predict transcription factor regulation enrichment analysis by chromatin immunoprecipitation-X enrichment analysis (ChEA)[36,37] (Figure 8A). The top predicted transcriptional regulator was an important regulator of astrogliogenesis, ATF3, followed by transcriptional repressor ZNF217 (Figure 8A). To validate this finding, we looked at protein levels of ATF3 by Western blot. Compared to control iAstros, HD iAstros had significantly decreased ATF3, suggesting that aberrant HD astrogliogenesis

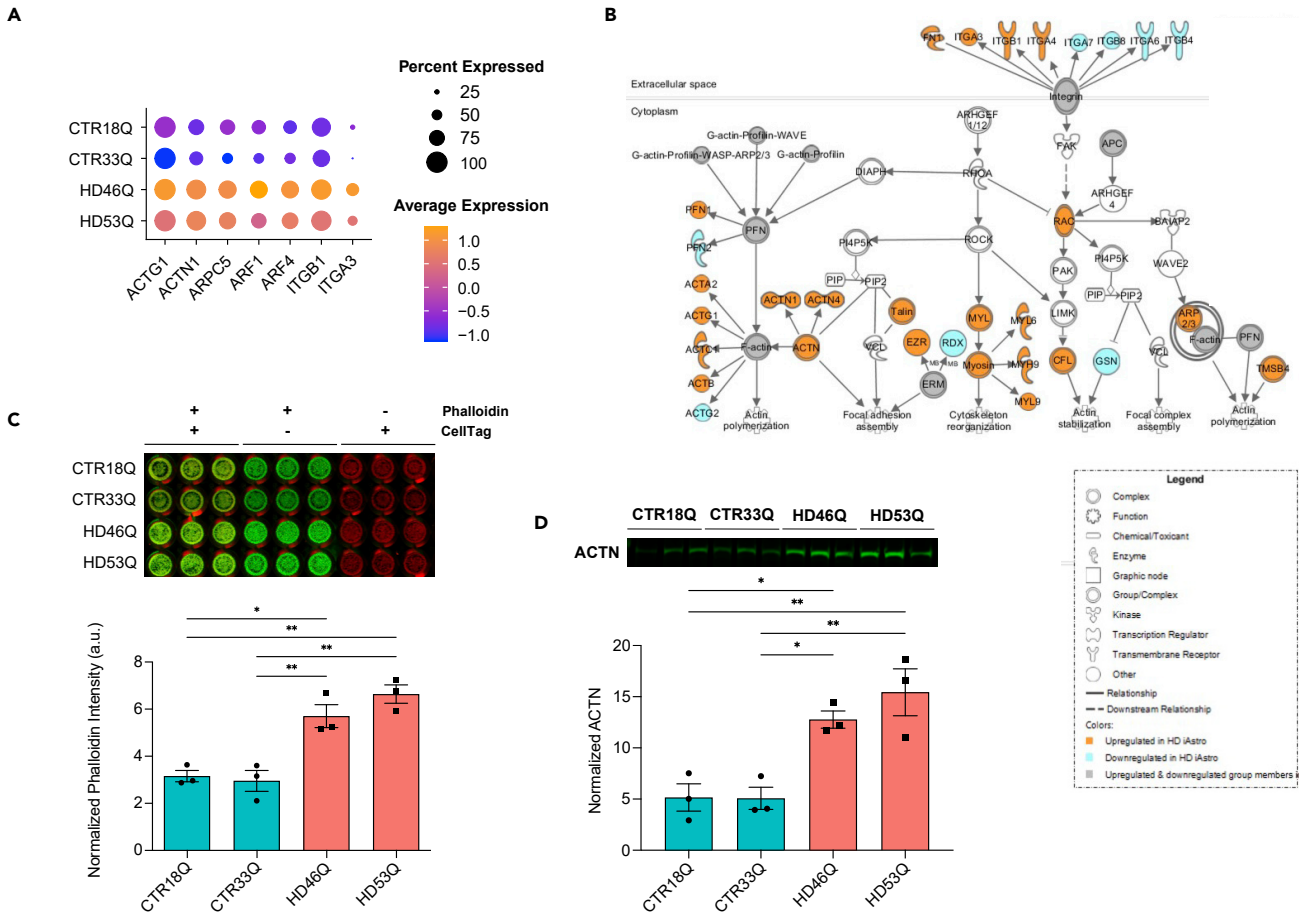

Figure 7. Actin cytoskeletal and integrin signaling activation in human HD iAstros

(A) Significantly downregulated molecules in integrin and actin cytoskeletal signaling pathways HD and control iAstro lines.

(B) Pathway or network from snRNAseq including ITGs and actin. Solid orange symbol represents upregulated DEG, and solid cyan symbol represents downregulated DEG.

(C) Phalloidin in-cell Western blot and quantification shows significant upregulation of F-actin in HD iAstro cell lines (one-way ANOVA: 18Qv46Q *$p < 0.05$; 33Qv46Q, 18Qv53Q, and 33Qv53Q: **$p < 0.01$; 18Qv33Q and 46Qv53Q: ns; n = 3 biological [differentiation] replicates per line, 2 lines per genotype).

(D) ACTN Western blot and quantification shows significant increased ACTN in HD iAstros (one-way ANOVA: 18Qv46Q and 33Qv46Q: *$p < 0.05$; 18Qv53Q and 33Qv53Q: **$p < 0.01$; 18Qv33Q and 46Qv53Q: ns; n = 3 biological [differentiation] replicates per line, 2 lines per genotype). All error bars indicate mean ± standard error mean. See also Data S1.

may be driven by known transcriptional regulators of this process (Figure 8B). Furthermore, SOX9, a transcriptional regulator of glial development and early astrogliogenesis, which was downregulated in HD iAstros, also had significantly decreased protein levels by Western blot (Figure 8C). The neural stem cell factor SOX2 was also enriched. YAP1 of the HIPPO signaling pathway that has an essential role in regeneration and self-renewal was another significantly enriched factor in HD iAstros that has previously been implicated in HD and shown to interact with Htt.[38] Overall, HD astrocyte transcriptionally dysregulated cell states and predicted alterations in transcription factors may implicate an astrogliogenesis deficit that induces astrocyte dysfunctions in glutamate signaling and activation of ECM and actin cytoskeletal signaling to potentially contribute to HD pathogenesis via altered glutamate uptake and cellular motility, respectively.

To identify possible transcriptional regulators in R6/2 astrocytes, we conducted transcription factor enrichment analysis[37] using the 56 common 12-week DEGs (Figure 5C and Data S2). The ChEA database showed glial developmental transcription factor, SOX9, as the most significant transcription factor enriched, suggesting a role for this complex in altered gene expression in R6/2 mouse astrocytes (Figure 8D). TCF4, a transcription factor involved in nervous system development, and SUZ12, a member of the polycomb repressive complex 2, were also enriched, suggesting roles for these complexes in repressing

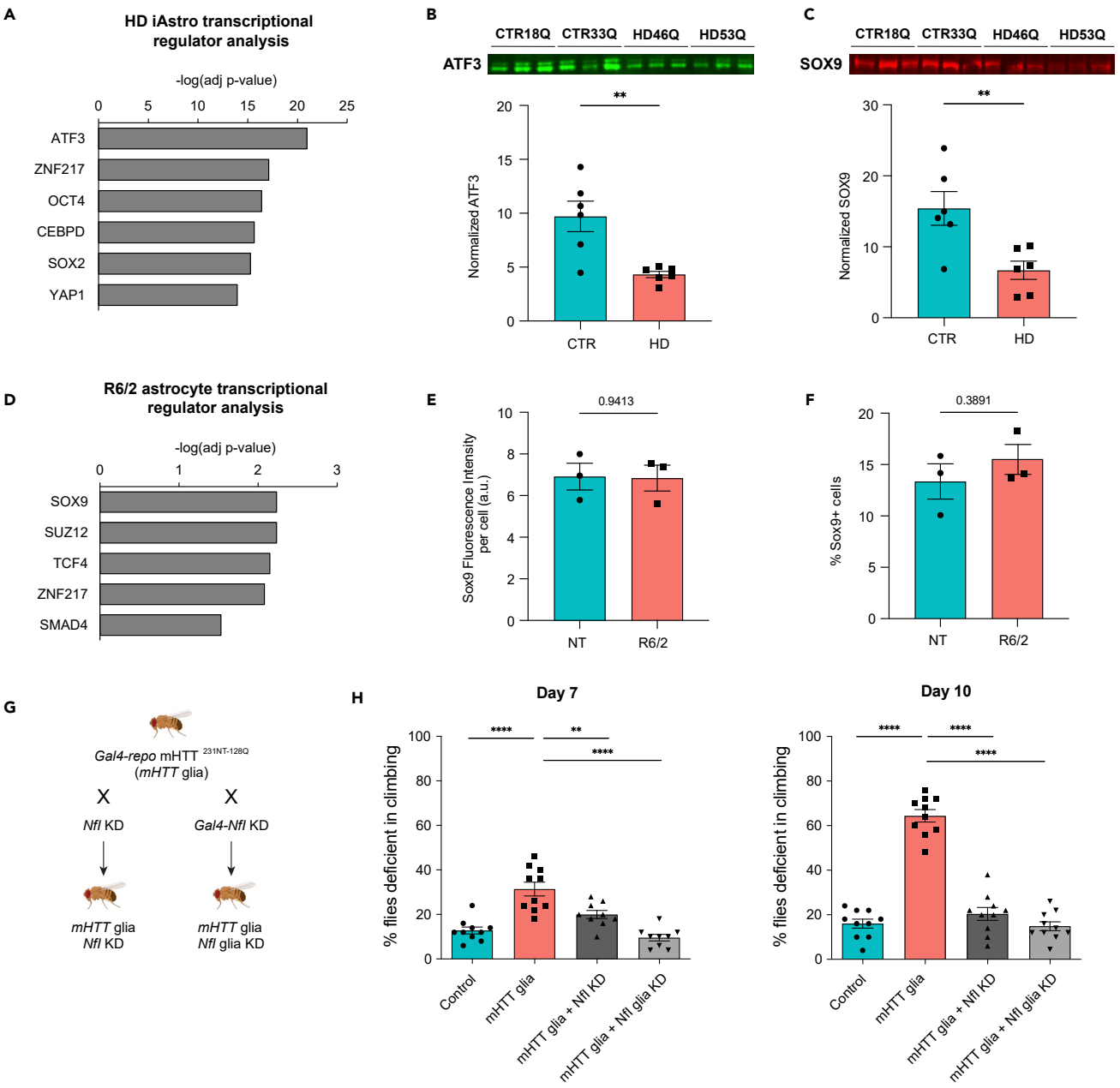

Figure 8. Transcriptional regulation of HD astrocytes by astrogliogenesis factors

(A) HD iAstros predicted transcription factor regulation analysis is enriched in developmental regulators.

(B and C) ATF3 (B) and SOX9 (C) Western blot and quantification shows significant decreased ATF3 (unpaired t-test: **p = 0.004, n = 3 biological [differentiation] replicates per line, 2 lines per genotype) and SOX9 (unpaired t-test: **p = 0.009, n = 3 biological [differentiation] replicates per line, 2 lines per genotype) in HD iAstros.

(D) Overlap of 12-week striatal and cortical astrocyte DEGs predicted transcription factor regulation in R6/2 astrocytes across both brain regions in symptomatic mice.

(E and F) Immunohistochemistry in non-transgenic (NT) or R6/2 mouse striatum shows no significant difference in intensity or number of GFAP-positive or S100β-positive cells astrocytes that express SOX9 (unpaired t-test: intensity ns, percentage cells ns, n = 3 mice per genotype with 16 images per mouse).

(G) An HD fragment Drosophila model ($HTT^{231NT128Q}$) was crossed with lines that reduce expression of Nfl, the fly ortholog to human NFIA, in glia using the Gal4 system.

(H) A climbing assay was performed at day 7 and day 10. When mHTT was expressed in glia (pink bar), flies demonstrate a temporal increase in climbing deficiency. When fly lines with reduced expression of Nfl were crossed with flies that express mHTT only in glia (dar and light gray bars), the climbing deficit was largely suppressed. Unpaired t-tests were performed comparing each line to the mHTT-expressing line within each dataset: ****p < 0.0001, **p = 0.01; n = 10 biological replicates, each containing 9–10 animals with 5 consecutive trials per replicate per day). All error bars indicate mean ± standard error mean.

astrogliogenesis genes in HD (Figure 8D), that have also been implicated in HD neurons,[39] endothelial genes in HD BMECs,[6,40] and HD oligodendroglia.[40] Another predicted transcriptional regulator in R6/2 astrocytes was the transcriptional repressor ZNF217, also present in HD iAstro analysis (Figures 8A and 8D). SOX9 protein expression was evaluated in the striatum of 10-week-old R6/2 mice; however, there was no significant change in expression levels or number of SOX9-expressing astrocytes (GFAP-positive or S100β-positive cells) (Figures 8E and 8F). For further investigation into transcription factor perturbation in R6/2 mouse astrocytes, Enrichr transcription factor database was queried (Figure S6B). Hes family bHLH transcription factor 1 (HES1) overexpression was implicated as the most significant perturbation, further implicating transcriptional repression of nervous system development in R6/2. Alterations in ASCL1 and MECP2, regulators of neural development, were also predicted to contribute to common dysregulated gene sets in R6/2 striatal and cortical astrocytes. NFIA, a transcription factor that controls astrogliogenesis, was identified as being deficient, indicating a potential mechanism for altered astrocyte development in R6/2. These findings highlight potential mechanisms in astrogliogenesis and neural developmental dysregulation contributing to downstream pathway dysregulation in mHTT-expressing astrocytes—a similar finding to our human iAstro model of HD.

Modulation of astrogliogenesis regulator NFIA/Nfl in HD drosophila glia is protective

Lastly, evaluated if perturbation of an astrogliogenesis transcriptional regulator can rescue HD astrocyte-induced deficits *in vivo*. The *Drosophila* model system was leveraged given the ease of genetic manipulation, short life cycle, and simple functional assays used to assess complex glial biology[43,44] as well as previous data showing a deficit in glia in HD model flies.[41,42] An HD fragment *Drosophila* model where mHTT ($HTT^{231NT128Q}$) is expressed in a pan-glia (*repo*) driver was crossed with lines that have a knockdown of the fly ortholog to human *NFIA*, *Nfl*. We used a general driver of mHTT in glia versus an astrocyte-specific driver, such as Alarm-Gal4, because of the robust phenotypes previously reported using repo-Gal4[42] and that a large proportion of cells targeted by the repo driver are astrocytes.[45] The astrogliogenesis transcriptional regulator, Nfl, was evaluated due to its high orthology prediction (DIOPT) score[46] with human NFIA and high activity in the larval ventral nerve chord, suggesting it may have an orthologous function in flies. Using a climbing assay,[41] mHTT flies exhibited a significant deficit in climbing compared to control flies (Figure 8G). The mHTT-induced climbing deficit was improved in lines with Nfl knockdown in all cells (*Nfl* KD) or in only glia (*Nfl* glia KD) by 7 days and rescued to control levels by 10 days (Figure 8G). Therefore, one of the astrogliogenesis transcriptional regulators predicted from dysregulated HD mouse and human astrocyte transcriptomic analysis demonstrates that perturbation of astrogliogenesis can improve HD functional deficits *in vivo*.

DISCUSSION

Unbiased single-cell approaches define cell states across the landscape of thousands of individual cells, providing a unique window into the cell states that arise during disease.[47] Cell types whose function span a wide range of biological processes, such as astrocytes, are ideal candidates for the investigation of cell state transitions in disease. The goal of our studies was to identify and compare astrocyte transcriptional cell states in specific systems and time points, their transitions in unaffected control and HD systems, and to elucidate the regulatory signaling involved. We investigated transcriptome signatures from human iPSC-derived astrocytes and astrocytes from a transgenic mouse model to elucidate common and species-specific cell states, as well as aberrant cell states that exist in both human and mouse HD astrocytes. Both models demonstrated potential loss of cell states involved in neural support, glutamate signaling, ion-binding, and neural development. Both also suggest astrocyte developmental alterations that are predicted to be regulated by astrogliogenesis transcription factors. HD human astrocytes exhibited a unique activation of ECM and cytoskeletal signaling that was not observed in R6/2 astrocytes. While most of the transcriptional cell states we identified in both human and mouse data were represented in HD and control samples, with shifts in percent composition in each condition, the HD iAstro data revealed complete loss of a unique control cell state that showed high expression of *NEAT1*, a gene associated with the stability of nuclear paraspeckles and thought to function through interactions with RNA binding and other proteins and RNAs, thus affecting transcription.[28,48] *NEAT1* has also been implicated in striatal neurons from patients with HD and mouse models, with its overexpression protecting from mHTT-induced cytotoxicity.[27] The R6/2 astrocytic dysregulation that overlapped between brain regions and with the human data showed an increase in severity between 8 and 12 weeks, suggesting that astrocyte dysregulation is progressive as described previously for bulk RNA-seq analysis of purified astrocytes[19]; however, there were unique differences found in 8-week cortical astrocytes involving SP1 signaling and lipid metabolism, which may

represent unique age-dependent cortical changes or early changes that give rise to the dysregulation of related molecular processes at 12 weeks. Overall, the dysregulated astrocytic states identified here are anticipated to induce dysfunctional brain homeostasis and contribute to HD pathogenesis.

Single-nuclei technology has allowed us to identify diverse astrocyte states within a heterogeneous astrocyte population through unsupervised computational clustering that may not have been identified using traditional bulk transcriptomic analysis.[49] Homeostatic astrocyte states identified from control iAstros and NT mouse astrocytes, compared to HD iAstros or R6/2 mouse astrocytes, included activation of signaling pathways previously suggested to play roles in astrocyte functions. Synaptogenesis signaling and CREB signaling were significantly activated in NT striatal and cortical astrocyte states along with calcium-binding activation in the cortex. In control human iAstros, several synaptogenesis-related genes were among the top upregulated cluster markers (*SPARCL1*) in control iAstro state cluster 0. Similarly, glutamate receptor signaling was significantly activated across an NT striatal mouse astrocyte state relative to R6/2 striatal astrocyte clusters. Overall, snRNA-seq analyses of control iAstros and non-transgenic mouse astrocytes were enriched with terms implicating synaptogenesis, glutamate signaling, and other neural supportive transcriptional cell states that are typical of homeostatic astrocytes.

HD human iAstro and R6/2 astrocyte phenotype comparisons

The commonly dysregulated astrocyte state across HD human iAstros and R6/2 mouse astrocytes was the inhibition of glutamate signaling. This phenotype is consistent with previous studies suggesting that glutamate handling is a critical feature of excitotoxicity in HD.[50–52] Astrocytes terminate the action of neurotransmitters, like glutamate and gamma-aminobutyric acid (GABA), through uptake at the tripartite synapse. In the case of glutamate, astrocytes help clear this excitatory neurotransmitter from the synaptic cleft through transporters (GLT1 and GLAST) and with the help of transmembrane glutamate receptors (GluR1 and GluR2) that form ligand-gated ion channels.[53–55] Within the cytosol of astrocytes, glutamate is then degraded into the neuro-inactive state, glutamine, via glutamine synthetase (GLUL) in an ATP-dependent manner; each of these were downregulated in our present study. These changes were validated by decreased protein levels of the glutamate transporter GLAST, in human HD iAstros upon FACS isolation, and AMPA glutamate receptor GluR1 in GLAST-positive HD iAstros compared to control. These alterations lead to functional impairment though decreased glutamate receptor signaling, which correlated with decreased glutamate uptake in HD iAstros. This dysregulation is present in R6/2 and other models of HD and may involve potassium ion channel Kir4.1 in R6/2 mice.[9,16,18,19,56–58] The evidence of dysfunctional glutamate regulation in our adult-onset HD iAstro lines is consistent with prior studies demonstrating a similar phenotype in juvenile-onset HD iPSC-derived astrocytes,[9] and with loss of GLT1 expression in mice with HTT-160Q selectively expressed only in astrocytes.[56] Our findings further support a cell-autonomous component of aberrant glutamate signaling inhibition in HD astrocytes with functional consequences in human cells.

Axonal guidance was an inhibited pathway predicted in one of the iAstro cell states composed largely of HD cells and overlapped with striatal R6/2 astrocyte cell states. This neural developmental pathway is necessary to guide neurons to their correct targets for proper synaptogenesis; therefore, inhibition of this critical process would alter neuronal circuitry homeostasis. Moreover, both iAstro cluster 3 and R6/2-enriched striatal cluster 4 appeared to be in a more immature, proliferative cell state. Aberrant activation of cell cycle-related signaling has been demonstrated in HD mice,[35,59] HD iPSC-derived neural models,[23,24,60,61] and HD patient tissue.[62,63] Osipovitch et al also demonstrated a decrease in GFAP expression in patient with HD embryonic stem cell-derived astrocytes that reflects impaired astrocytic differentiation.[7]

Developmental alterations in HD iAstros and decreased mature astrocyte markers in a striatal R6/2 astrocyte subpopulation may be a common cell state associated with mHTT-induced decreased astrogliogenesis. Transcription factor analysis and protein validation in HD iAstros identified downregulation of early astrogliogenesis factors: SOX9 and ATF3.[64,65] These genes may be driving maturation impairments in HD astrocytes, and subsequently causing alterations in astrocyte functions as these immature cell states also showed decreased expression of functional genes. HES1 overexpression was one of the most significantly enriched transcription factors in R6/2 12-week astrocytes along with the dysregulation of several HES genes in HD iAstros; this is consistent with epigenetic dysregulation of a HES family transcription factor (HES4) associated with striatal degeneration in HD postmortem cortex.[66] The observed molecular

phenotypes may also be due to a loss of astrocyte identity rather than a developmental alteration, as suggested in a previous study[67]; however, the human HD iAstros data suggest a developmental phenotype given the decreased propensity for HD iPSCs to differentiate into GLAST-positive, morphologically mature astrocytes, similar to altered *in vivo* astroglial differentiation of human glial progenitor cells from HD embryonic stem cells.[7] Both hypotheses could be occurring as HD progresses and mature cells lose their identity while progenitor cells give rise to developmentally impaired astrocytes. Nonetheless, alterations in astrocyte functions are likely, in part, due to the lack of mature astrocyte characteristics. Rescuing these deficits may require the proper induction of transcriptional regulators that are involved in the development and maturation of astrocytes and the expression of mature functional genes. Alternatively, persistent activation of developmental regulators may impede proper differentiation and maturation of HD astrocytes, which would require appropriate downregulation of these genes.

NFIA is a master astrogliogenesis transcriptional regulator that acts as a co-regulator with SOX9 in early astrogliogenesis[68] and ATF3 in later astrogliogenesis.[65] We assessed perturbation of NFIA in HD model animals. When the fly ortholog to human NFIA, Nfl, was knocked down in either all cells or in glia of a fly model of HD, the functional capacity for the mHTT repo flies to climb was significantly improved. An interpretation of this is that if a downregulated gene is knocked down and the phenotype is rescued, that gene may be downregulated as a compensatory mechanism.[42] Another interpretation may be due to the differences in timepoints assessed across the three HD models utilized in this study. The autophagic balance of these transcription factors, like many others in HD, may be altered differently depending on disease stage due to mHTT-induced alterations in clearance and accumulation of such proteins.[69–71] To this account, SOX9 was significantly decreased in HD iAstros and predicted to be a transcriptional regulator, but was not significantly decreased in R6/2 astrocytes. Investigations into additional timepoints across HD models are necessary for elucidation of this hypothesis. Overall, the astrogliogenesis transcriptional factors, like NFIA, are dysregulated across multiple HD models and can be targeted for improved functional outcomes in a model of HD.

Astrocyte reactivity has been documented in HD mouse[72–75] and human tissue[76,77]; however, the extent of cell-autonomous astrogliosis has not been extensively characterized. Surprisingly, control iAstros appeared to exhibit a more activated neuroinflammatory state compared to HD; however, this was a relatively small cell state in iAstro cluster 6, only encompassing 5% of the total nuclei sequenced. This suggests that control human iAstros may have a greater ability to mount normal inflammatory responses, including those that are a hallmark of *in vitro* cultured astrocytes.[78] Neuroinflammatory signaling was enriched in R6/2 striatal and cortical genotype-specific differentially expressed genes, with minor activation in striatal 12-week astrocytes; however, looking closely into the cell states, cortical cluster 4 and iAstro cluster 6 had a predicted activation of neuroinflammation signaling and had populations that shifted toward unaffected control or NT cells. Consistent with this hypothesis, R6/2-enriched striatal cluster 4, which had the lowest expression of mature astrocyte markers, had a predicted inhibition of neuroinflammatory signaling, demonstrating a potential loss of cell function in HD. These data suggest that both activated and inhibited neuroinflammatory states may exist in HD and could be playing different roles in the disease. Some of these neuroinflammatory states may only arise due to extrinsic signaling from other CNS cell types, as suggested by the lack of neuroinflammatory states in the HD iAstros. Since immune responses of astrocytes can induce detrimental and/or beneficial effects on neighboring cell types, it is unknown what consequences would result from loss of this cell state.[79] While a lack of inflammatory response in HD astrocytes contrasts with evidence in literature showing evidence of reactive astrocytes in HD mouse models[72–74] and human postmortem tissue,[57,72,75–77] more recent studies support a lack of traditional or A1-like reactive astrogliosis states in HD.[15,16,19,21]

Overall, there were several dysregulated pathways common to HD human iAstros and R6/2 astrocytes. Differences between systems may be due to multiple reasons, including expression of an expanded repeat HTT exon 1 transgene in R6/2, while HD iAstros contain the full-length endogenous mHTT. Recent studies identified similarities and differences across astrocytes from truncated (R6/2) and full-length (zQ175) mHTT mouse and human stem cell-derived models[10] or postmortem human striatal tissue.[19] Some similarities across mouse and human models in these studies and our study highlighted ion homeostasis, metabolism, neurotransmitter signaling (including glutamate receptor signaling), and astrocyte morphology.[10,19] Finally, species differences may also contribute as human astrocytes have greater development of astrocyte networks both in numbers and complexity, exhibiting significantly more multi-branched processes

than rodent astrocytes.[12,34] The increased ability of adult human astrocytes to respond to extracellular glutamate compared to mouse astrocytes is an example that suggests adult human astrocytes may have evolved an improved capability to respond to synaptic activity.[25,34,80]

Unique HD human iAstro phenotypes

Signaling states unique to human HD iAstros included activation of actin cytoskeletal and integrin signaling. Additionally, HD iAstros had a decrease in matrix metalloproteinases (*MMP15 & 17*) that aid in ECM degradation. Altered actin cytoskeletal dynamics was validated by increased Phalloidin (F-actin) staining and the actin crosslinking protein, ACTN, in HD iAstros at the protein level. This gain-of-function cell state unique to human HD iAstros compared to R6/2 astrocytes suggests a cellular state transition that is most likely a cell-autonomous effect, not influenced by the presence of other cell types that provide developmental cues for astrocytes. Altered actin cytoskeletal dynamics in HD have been implicated due to interaction with HTT, including the major actin monomer sequestering protein, profilin.[81–83] The functional relevance of actin and integrin activation to disease pathogenesis has yet to be determined but may relate to altered morphology, adhesion, intracellular trafficking, and transcriptional regulation.

Unique R6/2 astrocyte dysregulated cell states

Cyclic adenosine monophosphate (cAMP)-mediated signaling was the most inhibited pathway in striatal and cortical R6/2 astrocytes at 12 weeks. This signaling pathway plays a vital role in cellular signaling, including the regulation of glucose and lipid metabolism. *Phkg1* was a downregulated gene common across both timepoints and both brain regions, and was unique to R6/2. Since astrocytes are the primary storage site for glycogen in the brain,[84] a decrease in *Phkg1* would reduce glycogen phosphorylase's ability to break down glycogen in astrocytes needed for the high energy demand of neurons. Decreased glucose levels have been shown in HD astrocytes purified from mouse striatum.[85] Furthermore, decreased striatal metabolism in HD patients has been attributed to decreased glucose uptake through GLUT3.[86,87] In addition to disrupting neuronal activity, reduced glucose levels may impact downstream epigenetic and transcriptomic signatures.

We also described cellular states unique to the two brain regions assessed. Striatal R6/2 cell state differences highlighted changes in maturation and ion transport/binding astrocytic processes, while cortical R6/2 astrocytes mostly presented glycosylated cell state transition with an inhibited synaptogenesis signature. Striatal R6/2 astrocytes and HD iAstros clusters had a loss of astrocyte identity genes. This molecular phenotype was less overt in cortical R6/2 astrocytes with fewer significant differentially expressed genes across genotype for 12-week and 8-week cortical astrocytes compared to striatal, which yielded less diversity in significant pathway dysregulation. The differenes in molecular phenotype by brain region may correspond with more overt neurodegeneration in the striatum, compared to the cortex.

In summary, our findings indicate that aberrant cell states exist in individual HD astrocytes that include inhibition of glutamate signaling and potential developmental alterations that may be regulated by mutant HTT's interaction with astrogliogenesis transcription factors, ATF3, NFIA, and SOX9. In addition, loss of astrocyte maturation may contribute to inhibition of astrocytic functions, such as glutamate signaling, in human HD and R6/2 astrocytes. Knockdown of NFIA in HD flies rescued motor deficits and may suggest that restored protein levels of this key astrogliogenesis transcription factor would be neuroprotective, possibly by allowing glial cells to reach full maturity if the protein is functioning in the HD context. The identification of common and unique HD cell states across a heterogeneous population of human and mouse astrocytes provides directions for further mechanistic evaluation and greater information relating to potential therapeutic interventions targeting these dysregulated astrocytic states in HD as well as predicted outcomes across model systems.

Limitations of the study

In this study, iPSC-derived astrocytes were grown *in vitro* to mimic conditions of human astrocyte growth; however, this methodology results in early-stage astrocytes in 2D culture, therefore may lack signals and physical interaction from other neurovascular unit cell types that they would be exposed to *in vivo*. As discussed above, we interpret the HD iAstro results as potential cell-autonomous features of bona fide HD human astrocytes, and future studies are aimed at further investigating this hypothesis. Secondly, it is possible that differences in genetic background between HD and control patients may have confounded

the analysis across the non-isogenic HD iAstro lines analyzed. Nonetheless, we noted consistent dysregulated features across HD iAstros that were lacking in unaffected control iAstros, such as glutamate signaling downregulation and actin-related signaling upregulation, with some of these features recapitulated in HD mouse astrocytes. Additionally, male and female control iPSC lines were used in this study, while all male HD patient-derived iPSC lines were used for much of the analysis due to efficiency of differentiations and availability of lines. The data in this study were based on readouts from one to two timepoints and may not have captured subtle developmental and maturation-related features of HD astrocyte dysregulation. Lastly, the HD models assessed represent various disease stages and disease induction. For example, the R6/2 mouse is a rapidly progressing model of HD induced by the overexpression of the expanded CAG repeat-containing first exon of the mHTT gene, causing transcriptional deficits and severe motor dysfunction by 10–12 weeks of age and is representative of later stages of manifest disease. On the other hand, HD iAstros are generated from a pluripotent state in patient cells with endogenous full-length mHTT and are in a more developmentally immature state. Taken together, our results demonstrate astrocyte maturation deficits in multiple HD models that may influence dysregulated HD astrocyte cell states to induce dysfunctional astrocytic properties.

STAR★METHODS

Detailed methods are provided in the online version of this paper and include the following:

- KEY RESOURCES TABLE
- RESOURCE AVAILABILITY
  - Lead contact
  - Materials availability
  - Data and code availability
- EXPERIMENTAL MODEL AND SUBJECT DETAILS
  - iPSC lines and cell culture
  - Astrocyte differentiation
  - R6/2 mouse model
  - Fly husbandry
- METHOD DETAILS
  - FACS astrocyte-enrichment
  - Immunocytochemistry
  - Sholl and morphometric analysis
  - Glutamate uptake assay
  - F-actin in-cell western
  - Western blots
  - Single-nuclei RNA-sequencing
  - Data processing
  - Differential gene expression and pathway analysis
  - Immunohistochemistry and confocal microscopy
  - Fly climbing assay
- QUANTIFICATION AND STATISTICAL ANALYSIS

SUPPLEMENTAL INFORMATION

Supplemental information can be found online at https://doi.org/10.1016/j.isci.2022.105732.

ACKNOWLEDGMENTS

We thank patients with HD and their families for their essential contributions to this research. We acknowledge the UCI Stem Cell Research Flow Cytometry Core and specifically, Vanessa Scarfone and Pauline Nguyen, for their FACS technical assistance. We thank the technical assistance of Jennifer Stocksdale for expansion of iPSC lines utilized in this paper and Marie Heath for assistance with Western blot optimization. We are grateful to Dr. Juan Botas at Baylor College of Medicine for generously providing HD fly lines for this manuscript. We also acknowledge Drs. Peter Donovan, Suzanne Sandmeyer, and Jeff Rothstein for helpful discussions. This work was supported by the following NIH grants: R35 NS116872 (L.M.T.), R01834 NS089076 (L.M.T.) and associated Research Supplement award (A.M.R.), P01 NS092525 (L.M.T.), T32 Training Grant NS082174-05 (A.M.R.), 1RF1AG071683 (V.S.), and NS123207-01 (D.V.V.). Additional support from NSF Bridge to the Doctorate Fellowship (A.M.R.), UCI Stanley Behrens Family Foundation (A.M.R.),

UCI MIND startup funds (V.S.), CIRM Bridges to Stem Cell Program (C.J.S.), Hereditary Disease Foundation, Huntington's Disease Society of America, and the Huntington's Disease Community, Advocacy, Research & Education. This work was made possible in part, through access to the Genomics High-Throughput Facility Shared Resource of the Cancer Center Support Grant (P30CA-062203) at the University of California Irvine and NIH shared instrumentation grants: 1S10RR025496-01, 1S10OD010794-01, and 1S10OD021718-01. The graphical abstract was created with Biorender.com.

AUTHOR CONTRIBUTIONS

Conceptualization, A.M.R., R.G.L., and L.M.T.; Methodology, A.M.R., E.M.A., S.J.H., W.W.P., R.G.L., and L.M.T.; Formal Analysis, A.M.R., M.S.B., J.W., S.J.H., and R.G.L.; Investigation, A.M.R., M.S.B., S.J.H., N.G.M., K.Q.W., C.J.S., R.M., A.L., N.M., E.M., and J.C.R.; Resources, A.M.R., S.J.H., D.V.V., M.B.J., V.S., W.W.P., and L.M.T.; Data Curation, A.M.R., M.S.B., J.W., and R.G.L.; Writing – Original Draft, A.M.R.; Writing – Review & Editing, A.M.R., M.S.B., J.C.R., W.W.P., R.G.L., and L.M.T.; Visualization, A.M.R.; Supervision, R.G.L. and L.M.T.; Funding Acquisition, L.M.T.

DECLARATION OF INTERESTS

The authors declare no competing interests. Some authors have additional affiliations as noted below:

Andrea M. Reyes-Ortiz: Genentech, Inc., South San Francisco, California.

Edsel M. Abud: Scripps Research Translational Institute, La Jolla, California and Division of Allergy, Asthma, and Immunology, Scripps Clinic, San Diego, California.

Ryan G. Lim: Modulo Bio, Inc., San Diego, California.

Wayne W. Poon: NeuCyte, Inc., Mountain View, California.

Patent Pending: GENERATION AND APPLICATION OF FUNCTIONAL HUMAN ASTROCYTES FROM PLURIPOTENT STEM CELLS.

Inventors: Edsel Abud, Wayne Poon.

Received: July 1, 2022
Revised: October 13, 2022
Accepted: December 1, 2022
Published: January 20, 2023

REFERENCES

1. Macdonald, M. (1993). A novel gene containing a trinucleotide that is expanded and unstable on huntington's disease chromosomes. Cell *72*, 971–983.

2. Nance, M.A., and Myers, R.H. (2001). Juvenile onset Huntington's disease — clinical and research perspectives. Ment. Retard. Dev. Disabil. Res. Rev. *7*, 153–157. https://doi.org/10.1002/mrdd.1022.

3. Zuccato, C., Valenza, M., and Cattaneo, E. (2010). Molecular mechanisms and potential therapeutical targets in huntington's disease. Physiol. Rev. *90*, 905–981. https://doi.org/10.1152/physrev.00041.2009.

4. Bates, G.P., Dorsey, R., Gusella, J.F., Hayden, M.R., Kay, C., Leavitt, B.R., Nance, M., Ross, C.A., Scahill, R.I., Wetzel, R., et al. (2015). Huntington disease. Nat. Rev. Dis. Prim. *1*, 15005. https://doi.org/10.1038/nrdp.2015.5.

5. Ross, C.A., and Tabrizi, S.J. (2011). Huntington's disease: from molecular pathogenesis to clinical treatment. Lancet Neurol. *10*, 83–98. https://doi.org/10.1016/S1474-4422(10)70245-3.

6. Lim, R.G., Quan, C., Reyes-Ortiz, A.M., Lutz, S.E., Kedaigle, A.J., Gipson, T.A., Wu, J., Vatine, G.D., Stocksdale, J., Casale, M.S., et al. (2017). Huntington's disease iPSC-derived brain microvascular endothelial cells reveal WNT-mediated angiogenic and blood-brain barrier deficits. Cell Rep. *19*, 1365–1377. https://doi.org/10.1016/j.celrep.2017.04.021.

7. Osipovitch, M., Asenjo Martinez, A., Mariani, J.N., Cornwell, A., Dhaliwal, S., Zou, L., Chandler-Militello, D., Wang, S., Li, X., Benraiss, S.-J., et al. (2019). Human ESC-derived chimeric mouse models of huntington's disease reveal cell-intrinsic defects in glial progenitor cell differentiation. Cell Stem Cell *24*, 107–122.e7. https://doi.org/10.1016/j.stem.2018.11.010.

8. Juopperi, T.A., Kim, W.R., Chiang, C.H., Yu, H., Margolis, R.L., Ross, C.A., Ming, G.l., and Song, H. (2012). Astrocytes generated from patient induced pluripotent stem cells recapitulate features of Huntington's disease patient cells. Mol. Brain *5*, 17. https://doi.org/10.1186/1756-6606-5-17.

9. Garcia, V.J., Rushton, D.J., Tom, C.M., Allen, N.D., Kemp, P.J., Svendsen, C.N., et al. (2019). Huntington's disease patient-derived astrocytes display electrophysiological impairments and reduced neuronal support. Front. Neurosci. *13*, 669. https://doi.org/10.3389/fnins.2019.00669.

10. Benraiss, A., Mariani, J.N., Osipovitch, M., Cornwell, A., Windrem, M.S., Villanueva, C.B., Chandler-Militello, D., and Goldman, S.A. (2021). Cell-intrinsic glial pathology is

conserved across human and murine models of Huntington's disease. Cell Rep. *36*, 109308. https://doi.org/10.1016/j.celrep.2021.109308.

11. Zhao, Z., Nelson, A.R., Betsholtz, C., and Zlokovic, B. v (2015). Establishment and dysfunction of the blood-brain barrier. Cell *163*, 1064–1078. https://doi.org/10.1016/j.cell.2015.10.067.

12. Khakh, B.S., and Sofroniew, M.V. (2015). Diversity of astrocyte functions and phenotypes in neural circuits. Nat. Neurosci. *18*, 942–952. https://doi.org/10.1038/nn.4043.

13. Abbott, N.J., Rönnbäck, L., and Hansson, E. (2006). Astrocyte–endothelial interactions at the blood–brain barrier. Nat. Rev. Neurosci. *7*, 41–53. https://doi.org/10.1038/nrn1824.

14. Khakh, B.S., and Sofroniew, M.v. (2014). Astrocytes and Huntington's disease. ACS Chem. Neurosci. *5*, 494–496. https://doi.org/10.1021/cn500100r.

15. Tong, X., Ao, Y., Faas, G.C., Nwaobi, S.E., Xu, J., Haustein, M.D., Anderson, M.A., Mody, I., Olsen, M.L., Sofroniew, M.v., and Khakh, B.S. (2014). Astrocyte Kir4.1 ion channel deficits contribute to neuronal dysfunction in Huntington's disease model mice. Nat. Neurosci. *17*, 694–703. https://doi.org/10.1038/nn.3691.

16. Jiang, R., Diaz-Castro, B., Looger, L.L., and Khakh, B.S. (2016). Dysfunctional calcium and glutamate signaling in striatal astrocytes from huntington's disease model mice. J. Neurosci. *36*, 3453–3470. https://doi.org/10.1523/JNEUROSCI.3693-15.2016.

17. Milnerwood, A.J., Gladding, C.M., Pouladi, M.A., Kaufman, A.M., Hines, R.M., Boyd, J.D., Ko, R.W.Y., Vasuta, O.C., Graham, R.K., Hayden, M.R., et al. (2010). Early increase in extrasynaptic NMDA receptor signaling and expression contributes to phenotype onset in huntington's disease mice. Neuron *65*, 178–190. https://doi.org/10.1016/j.neuron.2010.01.008.

18. Lee, W., Reyes, R.C., Gottipati, M.K., Lewis, K., Lesort, M., Parpura, V., and Gray, M. (2013). Enhanced Ca2+-dependent glutamate release from astrocytes of the BACHD Huntington's disease mouse model. Neurobiol. Dis. *58*, 192–199. https://doi.org/10.1016/j.nbd.2013.06.002.

19. Diaz-Castro, B., Gangwani, M.R., Yu, X., Coppola, G., and Khakh, B.S. (2019). Astrocyte molecular signatures in Huntington's disease. Sci. Transl. Med. *11*, 8546. https://doi.org/10.1126/scitranslmed.aaw8546.

20. Hsiao, H.Y., Chen, Y.C., Huang, C.H., Chen, C.C., Hsu, Y.H., Chen, H.M., Chiu, F.L., Kuo, H.C., Chang, C., and Chern, Y. (2015). Aberrant astrocytes impair vascular reactivity in Huntington disease. Ann. Neurol. *78*, 178–192. https://doi.org/10.1002/ana.24428.

21. Al-Dalahmah, O., Sosunov, A.A., Shaik, A., Ofori, K., Liu, Y., Vonsattel, J.P., Adorjan, I., Menon, V., and Goldman, J.E. (2020). Single-nucleus RNA-seq identifies Huntington disease astrocyte states. Acta Neuropathol. Commun. *8*, 19. https://doi.org/10.1186/s40478-020-0880-6.

22. HD iPSC Consortium (2012). Induced pluripotent stem cells from patients with Huntington's disease show CAG-repeat-expansion-associated phenotypes. Cell Stem Cell *11*, 264–278. https://doi.org/10.1016/j.stem.2012.04.027.

23. HD iPSC Consortium (2017). Developmental alterations in Huntington's disease neural cells and pharmacological rescue in cells and mice. Nat. Neurosci. *20*, 648–660. https://doi.org/10.1038/nn.4532.

24. Smith-Geater, C., Hernandez, S.J., Lim, R.G., Adam, M., Wu, J., Stocksdale, J.T., Wassie, B.T., Gold, M.P., Wang, K.Q., Miramontes, R., et al. (2020). Aberrant development corrected in adult-onset huntington's disease iPSC-derived neuronal cultures via WNT signaling modulation. Stem Cell Rep. *14*, 406–419. https://doi.org/10.1016/j.stemcr.2020.01.015.

25. Vogel, H., Steinberg, G.K., Edwards, M.S.B., Caneda, C., Plaza, C.A., Blumenthal, P.D., Zhang, Y., Sloan, S.A., Clarke, L.E., Li, G., et al. (2016). Purification and characterization of progenitor and mature human astrocytes reveals transcriptional and functional differences with mouse. Neuron *89*, 37–53. https://doi.org/10.1016/j.neuron.2015.11.013.

26. Sunwoo, J.S., Lee, S.T., Im, W., Lee, M., Byun, J.I., Jung, K.H., Park, K.I., Jung, K.Y., Lee, S.K., Chu, K., and Kim, M. (2017). Altered expression of the long noncoding RNA NEAT1 in huntington's disease. Mol. Neurobiol. *54*, 1577–1586. https://doi.org/10.1007/s12035-016-9928-9.

27. Cheng, C., Spengler, R.M., Keiser, M.S., Monteys, A.M., Rieders, J.M., Ramachandran, S., and Davidson, B.L. (2018). The long non-coding RNA NEAT1 is elevated in polyglutamine repeat expansion diseases and protects from disease gene-dependent toxicities. Hum. Mol. Genet. *27*, 4303–4314. https://doi.org/10.1093/hmg/ddy331.

28. Hirose, T., Virnicchi, G., Tanigawa, A., Naganuma, T., Li, R., Kimura, H., Yokoi, T., Nakagawa, S., Bénard, M., Fox, A.H., and Pierron, G. (2014). NEAT1 long noncoding RNA regulates transcription via protein sequestration within subnuclear bodies. Mol. Biol. Cell *25*, 169–183. https://doi.org/10.1091/mbc.E13-09-0558.

29. Katsel, P., Roussos, P., Fam, P., Khan, S., Tan, W., Hirose, T., Nakagawa, S., Pletnikov, M. v, and Haroutunian, V. (2019). The expression of long noncoding RNA NEAT1 is reduced in schizophrenia and modulates oligodendrocytes transcription. NPJ Schizophr. *5*, 3. https://doi.org/10.1038/s41537-019-0071-2.

30. Hodges, A., Strand, A.D., Aragaki, A.K., Kuhn, A., Sengstag, T., Hughes, G., Elliston, L.A., Hartog, C., Goldstein, D.R., Thu, D., et al. (2006). Regional and cellular gene expression changes in human Huntington's disease brain. Hum. Mol. Genet. *15*, 965–977. https://doi.org/10.1093/hmg/ddl013.

31. Mangiarini, L., Sathasivam, K., Seller, M., Cozens, B., Harper, A., Hetherington, C., Lawton, M., Trottier, Y., Lehrach, H., Davies, S.W., and Bates, G.P. (1996). Exon 1 of the HD gene with an expanded CAG repeat is sufficient to cause a progressive neurological phenotype in transgenic mice. Cell *87*, 493–506. https://doi.org/10.1016/s0092-8674(00)81369-0.

32. Lim, R.G., Al-Dalahmah, O., Wu, J.M., Gold, M.P., Reidling, J.C., Tang, G., Adam, M., Dansu, D., Park, H.J., Casaccia, P., et al. (2022). Single nuclei RNAseq analysis of HD mouse models and human brain reveals impaired oligodendrocyte maturation and potential role for thiamine metabolism. Preprint at bioRxiv. https://doi.org/10.1101/2022.06.27.497613.

33. Zhang, Y., Chen, K., Sloan, S.A., Bennett, M.L., Scholze, A.R., O'Keeffe, S., Phatnani, H.P., Guarnieri, P., Caneda, C., Ruderisch, N., et al. (2014). An RNA-sequencing transcriptome and splicing database of glia, neurons, and vascular cells of the cerebral cortex. J. Neurosci. *34*, 11929–11947. https://doi.org/10.1523/JNEUROSCI.1860-14.2014.

34. Oberheim, N.A., Takano, T., Han, X., He, W., Lin, J.H.C., Wang, F., Xu, Q., Wyatt, J.D., Pilcher, W., Ojemann, J.G., et al. (2009). Uniquely hominid features of adult human astrocytes. J. Neurosci. *29*, 3276–3287. https://doi.org/10.1523/JNEUROSCI.4707-08.2009.

35. Luthi-Carter, R., Hanson, S.A., Strand, A.D., Bergstrom, D.A., Chun, W., Peters, N.L., Woods, A.M., Chan, E.Y., Kooperberg, C., Krainc, D., et al. (2002). Dysregulation of gene expression in the R6/2 model of polyglutamine disease: parallel changes in muscle and brain. Hum. Mol. Genet. *11*, 1911–1926. https://doi.org/10.1093/hmg/11.17.1911.

36. Chen, E.Y., Tan, C.M., Kou, Y., Duan, Q., Wang, Z., Meirelles, G.V., Clark, N.R., and Ma'ayan, A. (2013). Enrichr: interactive and collaborative HTML5 gene list enrichment analysis tool. BMC Bioinf. *14*, 128. https://doi.org/10.1186/1471-2105-14-128.

37. Kuleshov, M.v., Jones, M.R., Rouillard, A.D., Fernandez, N.F., Duan, Q., Wang, Z., Koplev, S., Jenkins, S.L., Jagodnik, K.M., Lachmann, A., et al. (2016). Enrichr: a comprehensive gene set enrichment analysis web server 2016 update. Nucleic Acids Res. *44*, W90–W97. https://doi.org/10.1093/nar/gkw377.

38. Mueller, K.A., Glajch, K.E., Huizenga, M.N., Wilson, R.A., Granucci, E.J., Dios, A.M., Tousley, A.R., Iuliano, M., Weisman, E., Laquaglia, M.J., et al. (2018). Hippo signaling pathway dysregulation in human huntington's disease brain and neuronal stem cells. Sci. Rep. *8*, 11355. https://doi.org/10.1038/s41598-018-29319-4.

39. Seong, I.S., Woda, J.M., Song, J.-J., Lloret, A., Abeyrathne, P.D., Woo, C.J., Gregory, G., Lee, J.-M., Wheeler, V.C., Walz, T., et al. (2010). Huntingtin facilitates polycomb repressive complex 2. Hum. Mol. Genet. *19*, 573–583. https://doi.org/10.1093/hmg/ddp524.

40. Ferrari Bardile, C., Garcia-Miralles, M., Caron, N.S., Rayan, N.A., Langley, S.R., Harmston, N., Rondelli, A.M., Teo, R.T.Y., Waltl, S., Anderson, L.M., et al. (2019). Intrinsic mutant HTT-mediated defects in oligodendroglia cause myelination deficits and behavioral abnormalities in Huntington disease. Proc. Natl. Acad. Sci. USA *116*, 9622–9627. https://doi.org/10.1073/pnas.1818042116.

41. Al-Ramahi, I., Lu, B., di Paola, S., Pang, K., de Haro, M., Peluso, I., Gallego-Flores, T., Malik, N.T., Erikson, K., Bleiberg, B.A., et al. (2018). High-throughput functional analysis distinguishes pathogenic, nonpathogenic, and compensatory transcriptional changes in neurodegeneration. Cell Syst. *7*, 28–40.e4. https://doi.org/10.1016/j.cels.2018.05.010.

42. Onur, T.S., Laitman, A., Zhao, H., Keyho, R., Kim, H., Wang, J., Mair, M., Wang, H., Li, L., Perez, A., et al. (2021). Downregulation of glial genes involved in synaptic function mitigates huntington's disease pathogenesis. Elife *10*, e64564. https://doi.org/10.7554/eLife.64564.

43. Freeman, M.R., and Doherty, J. (2006). Glial cell biology in Drosophila and vertebrates. Trends Neurosci. *29*, 82–90. https://doi.org/10.1016/j.tins.2005.12.002.

44. Ziegenfuss, J.S., Doherty, J., and Freeman, M.R. (2012). Distinct molecular pathways mediate glial activation and engulfment of axonal debris after axotomy. Nat. Neurosci. *15*, 979–987. https://doi.org/10.1038/nn.3135.

45. Stork, T., Bernardos, R., and Freeman, M.R. (2012). Analysis of glial cell development and function in Drosophila. Cold Spring Harb. Protoc. *2012*, 1–17. https://doi.org/10.1101/pdb.top067587.

46. Hu, Y., Flockhart, I., Vinayagam, A., Bergwitz, C., Berger, B., Perrimon, N., and Mohr, S.E. (2011). An integrative approach to ortholog prediction for disease-focused and other functional studies. BMC Bioinf. *12*, 357. https://doi.org/10.1186/1471-2105-12-357.

47. Trapnell, C. (2015). Defining cell types and states with single-cell genomics. Genome Res. *25*, 1491–1498. https://doi.org/10.1101/gr.190595.115.

48. Clemson, C.M., Hutchinson, J.N., Sara, S.A., Ensminger, A.W., Fox, A.H., Chess, A., and Lawrence, J.B. (2009). An architectural role for a nuclear noncoding RNA: NEAT1 RNA is essential for the structure of paraspeckles. Mol. Cell *33*, 717–726. https://doi.org/10.1016/j.molcel.2009.01.026.

49. Hu, X., Yuan, Y., Wang, D., and Su, Z. (2016). Heterogeneous astrocytes: active players in CNS. Brain Res. Bull. *125*, 1–18. https://doi.org/10.1016/j.brainresbull.2016.03.017.

50. Choi, D.W. (1988). Glutamate neurotoxicity and diseases of the nervous system. Neuron *1*, 623–634. https://doi.org/10.1016/0896-6273(88)90162-6.

51. Cross, A.J., Slater, P., and Reynolds, G.P. (1986). Reduced high-affinity glutamate uptake sites in the brains of patients with huntington's disease. Neurosci. Lett. *67*, 198–202. https://doi.org/10.1016/0304-3940(86)90397-6.

52. Greenamyre, J.T. (1986). The role of glutamate in neurotransmission and in neurologic disease. Arch. Neurol. *43*, 1058–1063. https://doi.org/10.1001/archneur.1986.00520100062016.

53. Rothstein, J.D., Martin, L., Levey, A.I., Dykes-Hoberg, M., Jin, L., Wu, D., Nash, N., and Kuncl, R.W. (1994). Localization of neuronal and glial glutamate transporters. Neuron *13*, 713–725. https://doi.org/10.1016/0896-6273(94)90038-8.

54. Lehre, K.P., Levy, L.M., Ottersen, O.P., Storm-Mathisen, J., and Danbolt, N.C. (1995). Differential expression of two glial glutamate transporters in the rat brain: quantitative and Immunocytochemical observations. J. Neurosci. *15*, 1835–1853. https://doi.org/10.1523/JNEUROSCI.15-03-01835.

55. Rothstein, J.D., Dykes-Hoberg, M., Pardo, C.A., Bristol, L.A., Jin, L., Kuncl, R.W., Kanai, Y., Hediger, M.A., Wang, Y., Schielke, J.P., and Welty, D.F. (1996). Knockout of glutamate transporters reveals a major role for astroglial transport in excitotoxicity and clearance of glutamate. Neuron *16*, 675–686. https://doi.org/10.1016/s0896-6273(00)80086-0.

56. Bradford, J., Shin, J.Y., Roberts, M., Wang, C.E., Li, X.J., and Li, S. (2009). Expression of mutant huntingtin in mouse brain astrocytes causes age-dependent neurological symptoms. Proc. Natl. Acad. Sci. USA *106*, 22480–22485. https://doi.org/10.1073/pnas.0911503106.

57. Faideau, M., Kim, J., Cormier, K., Gilmore, R., Welch, M., Auregan, G., Dufour, N., Guillermier, M., Brouillet, E., Hantraye, P., et al. (2010). In vivo expression of polyglutamine-expanded huntingtin by mouse striatal astrocytes impairs glutamate transport: a correlation with Huntington's disease subjects. Hum. Mol. Genet. *19*, 3053–3067. https://doi.org/10.1093/hmg/ddq212.

58. Khakh, B.S., Beaumont, V., Cachope, R., Munoz-Sanjuan, I., Goldman, S.A., and Grantyn, R. (2017). Unravelling and exploiting astrocyte dysfunction in huntington's disease. Trends Neurosci. *40*, 422–437. https://doi.org/10.1016/j.tins.2017.05.002.

59. Conforti, P., Camnasio, S., Mutti, C., Valenza, M., Thompson, M., Fossale, E., Zeitlin, S., MacDonald, M.E., Zuccato, C., and Cattaneo, E. (2013). Lack of huntingtin promotes neural stem cells differentiation into glial cells while neurons expressing huntingtin with expanded polyglutamine tracts undergo cell death. Neurobiol. Dis. *50*, 160–170. https://doi.org/10.1016/j.nbd.2012.10.015.

60. Mattis, V.B., Tom, C., Akimov, S., Saeedian, J., Østergaard, M.E., Southwell, A.L., Doty, C.N., Ornelas, L., Sahabian, A., Lenaeus, L., et al. (2015). HD iPSC-derived neural progenitors accumulate in culture and are susceptible to BDNF withdrawal due to glutamate toxicity. Hum. Mol. Genet. *24*, 3257–3271. https://doi.org/10.1093/hmg/ddv080.

61. Ring, K.L., An, M.C., Zhang, N., O'Brien, R.N., Ramos, E.M., Gao, F., Atwood, R., Bailus, B.J., Melov, S., Mooney, S.D., et al. (2015). Genomic analysis reveals disruption of striatal neuronal development and therapeutic targets in human huntington's disease neural stem cells. Stem Cell Rep. *5*, 1023–1038. https://doi.org/10.1016/j.stemcr.2015.11.005.

62. Hickman, R.A., Faust, · P.L., Rosenblum, · M.K., Marder, · K., Mehler, · M.F., Vonsattel, · J.P., and Purpura, D.P. (2021). Developmental malformations in Huntington disease: neuropathologic evidence of focal neuronal migration defects in a subset of adult brains. Acta Neuropathol. *141*, 399–413. https://doi.org/10.1007/s00401-021-02269-4.

63. Barnat, M., Capizzi, M., Aparicio, E., Boluda, S., Wennagel, D., Kacher, R., Kassem, R., Lenoir, S., Agasse, F., Braz, B.Y., et al. (2020). Huntington's disease alters human neurodevelopment. Science *369*, 787–793. https://doi.org/10.1126/science.aax3338.

64. Kang, P., Lee, H.K., Glasgow, S.M., Finley, M., Donti, T., Gaber, Z.B., Graham, B.H., Foster, A.E., Novitch, B.G., Gronostajski, R.M., and Deneen, B. (2012). Sox9 and NFIA coordinate a transcriptional regulatory cascade during the initiation of gliogenesis. Neuron *74*, 79–94. https://doi.org/10.1016/j.neuron.2012.01.024.

65. Tiwari, N., Pataskar, A., Péron, S., Thakurela, S., Sahu, S.K., Figueres-Oñate, M., Marichal, N., López-Mascaraque, L., Tiwari, V.K., and Berninger, B. (2018). Stage-specific transcription factors drive astrogliogenesis by remodeling gene regulatory landscapes. Cell Stem Cell *23*, 557–571.e8. https://doi.org/10.1016/j.stem.2018.09.008.

66. Bai, G., Cheung, I., Shulha, H.P., Coelho, J.E., Li, P., Dong, X., Jakovcevski, M., Wang, Y., Grigorenko, A., Jiang, Y., et al. (2015). Epigenetic dysregulation of hairy and enhancer of split 4 (HES4) is associated with striatal degeneration in postmortem Huntington brains. Hum. Mol. Genet. *24*, 1441–1456. https://doi.org/10.1093/hmg/ddu561.

67. Langfelder, P., Cantle, J.P., Chatzopoulou, D., Wang, N., Gao, F., Al-Ramahi, I., Lu, X.H., Ramos, E.M., El-Zein, K., Zhao, Y., et al. (2016). Integrated genomics and proteomics define huntingtin CAG length-dependent networks in mice. Nat. Neurosci. *19*, 623–633. https://doi.org/10.1038/nn.4256.

68. Stevanovic, M., Drakulic, D., Lazic, A., Ninkovic, D.S., Schwirtlich, M., and Mojsin, M. (2021). SOX transcription factors as important regulators of neuronal and glial differentiation during nervous system development and adult neurogenesis. Front. Mol. Neurosci. *14*, 654031. https://doi.org/10.3389/fnmol.2021.654031.

69. Hernandez, S.J., Fote, G., Reyes-Ortiz, A.M., Steffan, J.S., and Thompson, L.M. (2021). Cooperation of cell adhesion and autophagy in the brain: functional roles in development and neurodegenerative disease. Matrix Biol. Plus *12*, 100089. https://doi.org/10.1016/j.mbplus.2021.100089.

70. Ochaba, J., Lukacsovich, T., Csikos, G., Zheng, S., Margulis, J., Salazar, L., Mao, K., Lau, A.L., Yeung, S.Y., Humbert, S., et al. (2014). Potential function for the Huntingtin protein as a scaffold for selective autophagy. Proc. Natl. Acad. Sci. USA *111*, 16889–16894. https://doi.org/10.1073/pnas.1420103111.

71. Jia, H., Kast, R.J., Steffan, J.S., and Thomas, E.A. (2012). Selective histone deacetylase (HDAC) inhibition imparts beneficial effects in Huntington's disease mice: implications for the ubiquitin-proteasomal and autophagy systems. Hum. Mol. Genet. *21*, 5280–5293. https://doi.org/10.1093/hmg/dds379.

72. Reddy, P.H., Williams, M., Charles, V., Garrett, L., Pike-Buchanan, L., Whetsell, W.O., Miller, G., and Tagle, D.A. (1998). Behavioural abnormalities and selective neuronal loss in HD transgenic mice expressing mutated full-length HD cDNA. Nat. Genet. *20*, 198–202. https://doi.org/10.1038/2510.

73. Lin, C.H., Tallaksen-Greene, S., Chien, W.M., Cearley, J.A., Jackson, W.S., Crouse, A.B., Ren, S., Li, X.J., Albin, R.L., and Detloff, P.J. (2001). Neurological abnormalities in a knock-in mouse model of Huntington's disease. Hum. Mol. Genet. *10*, 137–144. https://doi.org/10.1093/hmg/10.2.137.

74. Yu, Z.-X., Li, S.-H., Evans, J., Pillarisetti, A., Li, H., and Li, X.-J. (2003). Mutant huntingtin causes context-dependent neurodegeneration in mice with Huntington's disease. J. Neurosci. *23*, 2193–2202. https://doi.org/10.1523/JNEUROSCI.23-06-02193.2003.

75. Myers, R.H., Vonsattel, J.P., Paskevich, P.A., Kiely, D.K., Stevens, T.J., Cupples, L.A., Richardson, E.P., Jr., and Bird, E.D. (1991). Decreased neuronal and increased oligodendroglial densities in Huntington's disease caudate nucleus. J. Neuropathol. Exp. Neurol. *50*, 729–742. https://doi.org/10.1097/00005072-199111000-00005.

76. Sapp, E., Kegel, K.B., Aronin, N., Hashikawa, T., Uchiyama, Y., Tohyama, K., Bhide, P.G., Vonsattel, J.P., and Difiglia, M. (2001). Early and progressive accumulation of reactive microglia in the Huntington disease brain. J. Neuropathol. Exp. Neurol. *60*, 161–172. https://doi.org/10.1093/jnen/60.2.161.

77. Selkoe, D.J., Salazar, F.J., Abraham, C., and Kosik, K.S. (1982). Huntington's disease: changes in striatal proteins reflect astrocytic gliosis. Brain Res. *245*, 117–125. https://doi.org/10.1016/0006-8993(82)90344-4.

78. Ben Haim, L., Carrillo-de Sauvage, M.A., Ceyzériat, K., and Escartin, C. (2015). Elusive roles for reactive astrocytes in neurodegenerative diseases. Front. Cell. Neurosci. *9*, 278. https://doi.org/10.3389/fncel.2015.00278.

79. Ding, Z.B., Song, L.J., Wang, Q., Kumar, G., Yan, Y.Q., and Ma, C.G. (2021). Astrocytes: a double-edged sword in neurodegenerative diseases. Neural Regen. Res. *16*, 1702–1710. https://doi.org/10.4103/1673-5374.306064.

80. Sun, W., McConnell, E., Pare, J.-F., Xu, Q., Chen, M., Peng, W., Lovatt, D., Han, X., Smith, Y., and Nedergaard, M. (2013). Glutamate-dependent neuroglial calcium signaling differs between young and adult brain. Science *339*, 197–200. https://doi.org/10.1126/science.1226740.

81. Burnett, B.G., Andrews, J., Ranganathan, S., Fischbeck, K.H., and di Prospero, N.A. (2008). Expression of expanded polyglutamine targets profilin for degradation and alters actin dynamics. Neurobiol. Dis. *30*, 365–374. https://doi.org/10.1016/j.nbd.2008.02.007.

82. Harjes, P., and Wanker, E.E. (2003). The hunt for huntingtin function: interaction partners tell many different stories. Trends Biochem. Sci. *28*, 425–433. https://doi.org/10.1016/S0968-0004(03)00168-3.

83. Goehler, H., Lalowski, M., Stelzl, U., Waelter, S., Stroedicke, M., Worm, U., Droege, A., Lindenberg, K.S., Knoblich, M., Haenig, C., et al. (2005). A protein interaction network links GIT1, an enhancer of Huntingtin aggregation, to Huntington's disease. Mol. Cell *19*, 287. https://doi.org/10.1016/j.molcel.2005.06.031.

84. Sofroniew, M. v, and Vinters, H. v (2010). Astrocytes: biology and pathology. Acta Neuropathol. *119*, 7–35. https://doi.org/10.1007/s00401-009-0619-8.

85. Polyzos, A.A., Lee, D.Y., Datta, R., Hauser, M., Budworth, H., Holt, A., Mihalik, S., Goldschmidt, P., Frankel, K., Trego, K., et al. (2019). Metabolic reprogramming in astrocytes distinguishes region-specific neuronal susceptibility in huntington mice. Cell Metabol. *29*, 1258–1273.e11. https://doi.org/10.1016/j.cmet.2019.03.004.

86. Ciarmiello, A., Cannella, M., Lastoria, S., Simonelli, M., Frati, L., Rubinsztein, D.C., and Squitieri, F. (2006). Brain white-matter volume loss and glucose hypometabolism precede the clinical symptoms of huntington's disease. J. Nucl. Med. *47*, 216–222.

87. McClory, H., Williams, D., Sapp, E., Gatune, L.W., Wang, P., DiFiglia, M., and Li, X. (2014). Glucose transporter 3 is a rab11-dependent trafficking cargo and its transport to the cell surface is reduced in neurons of CAG140 Huntington's disease mice. Acta Neuropathol. Commun. *2*, 179. https://doi.org/10.1186/s40478-014-0178-7.

88. Chen, Y., Stevens, B., Chang, J., Milbrandt, J., Barres, B.A., and Hell, J.W. (2008). NS21: Re-defined and modified supplement B27 for neuronal cultures. J. Neurosci. Methods *171*, 239–247. https://doi.org/10.1016/j.jneumeth.2008.03.013.

89. Agrawal, N., Pallos, J., Slepko, N., Apostol, B.L., Bodai, L., Chang, L.-W., Chiang, A.-S., Thompson, L.M., and Marsh, J.L. (2005). Identification of combinatorial drug regimens for treatment of Huntington's disease using Drosophila. Proc. Natl. Acad. Sci. USA *102*, 3777–3781. https://doi.org/10.1073/pnas.0500055102.

90. Carpenter, A.E., Jones, T.R., Lamprecht, M.R., Clarke, C., Kang, I.H., Friman, O., Guertin, D.A., Chang, J.H., Lindquist, R.A., Moffat, J., et al. (2006). CellProfiler: image analysis software for identifying and quantifying cell phenotypes. Genome Biol. *7*, R100. https://doi.org/10.1186/gb-2006-7-10-r100.

91. Arshadi, C., Günther, U., Eddison, M., Harrington, K.I.S., and Ferreira, T.A. (2021). SNT: a unifying toolbox for quantification of neuronal anatomy. Nat. Methods *18*, 374–377. https://doi.org/10.1038/s41592-021-01105-7.

92. Ferreira, T.A., Blackman, A. v, Oyrer, J., Jayabal, S., Chung, A.J., Watt, A.J., Sjöström, P.J., and van Meyel, D.J. (2014). Neuronal morphometry directly from bitmap images. Nat. Methods *11*, 982–984. https://doi.org/10.1038/nmeth.

93. Sholl, D.A. (1953). Dendritic organization in the neurons of the visual and motor cortices of the cat. J. Anat. *87*, 387–406.

94. Stuart, T., Butler, A., Hoffman, P., Hafemeister, C., Papalexi, E., Mauck, W.M., Hao, Y., Stoeckius, M., Smibert, P., and Satija, R. (2019). Comprehensive integration of single-cell data. Cell *177*, 1888–1902.e21. https://doi.org/10.1016/j.cell.2019.05.031.

STAR★METHODS

KEY RESOURCES TABLE

REAGENT or RESOURCE	SOURCE	IDENTIFIER
Antibodies		
Mouse anti-OCT4	Millipore	Cat#MAB4401; RRID: AB_2167852
Rabbit anti-SOX2	Millipore	Cat#AB5603; RRID: AB_2286686
Mouse anti-Nestin	Millipore	Cat#MAB5326; RRID: AB_2251134
Rabbit anti-PAX6	Abcam	Cat#ab5790; RRID: AB_305110
Guinea pig anti-DCX	Millipore	Cat#AB2253; RRID: AB_1586992
Mouse anti-TUJ1	Millipore	Cat#MAB5564; RRID: AB_570921
Guinea pig anti-MAP2	Synaptic Systems	Cat#188004; RRID: AB_2138181
Chicken anti-GFAP	Abcam	Cat#ab4674; RRID: AB_304558
Rabbit anti-ALDH1L1	Abcam	Cat#ab87117; RRID: AB_10712968
Mouse anti-S100β	Abcam	Cat#ab4066; RRID: AB_304258
Mouse anti-GLAST	Miltenyi Biotec	Cat#130-095-822; RRID: AB_10829302
Mouse anti-GLAST-APC	Miltenyi Biotec	Cat#130-123-555; RRID: AB_2811532
Rabbit anti-AQP4	Abcam	Cat#ab81355; RRID: AB_1640202
Mouse anti-GluR1	Abcam	Cat#ab174785; RRID: AB_2920893
Rabbit anti-ATF3	Abcam	Cat#ab254268; RRID: AB_2910214
Mouse anti-IgG	Invitrogen	Cat#02–6502; RRID: AB_2532951
Rabbit anti-IgG	Invitrogen	Cat#02–6102; RRID: AB_2532938
Mouse anti-GluR1	Abcam	Cat#ab174785; RRID: AB_2920893
Mouse anti-ACTN	Sigma-Aldrich	Cat#A5044; RRID: AB_476737
Rabbit anti-ATF3	Abcam	Cat#ab254268; RRID: AB_2910214
Rabbit anti-SOX9	Sigma-Aldrich	Cat#AB5535; RRID: AB_2239761
Mouse anti-S100β	Sigma-Aldrich	Cat#S2532; RRID: AB_477499
IRDye® 700CW Goat anti-Rabbit IgG	LI-COR Biosciences	Cat#926–68071; RRID: AB_10956166
IRDye® 800CW Goat anti-Mouse IgG	LI-COR Biosciences	Cat#926–32210; RRID: AB_621842
IRDye® 800CW Goat anti-Rabbit IgG	LI-COR Biosciences	Cat#926–32211; RRID: AB_621843
Chemicals, peptides, and recombinant proteins		
Human Recombinant LIF	STEMCELL Technologies	Cat#78055
Human Recombinant CNTF	Peprotech	Cat#450–13
Human Recombinant bFGF	STEMCELL Technologies	Cat#78003.2
N-Acetylcysteine	Sigma-Aldrich	Cat#A9165
Human Recombinant HBEGF	R&D Systems	Cat#259-HE
Critical commercial assays		
Glutamate Assay Kit	Abcam	Cat#ab83389
Phalloidin-iFluor790	Abcam	Cat#ab176763
Deposited data		
Human iPSC-derived astrocyte snRNA-seq raw and analyzed data	This paper	GEO: GSE214973
Full mouse snRNA-seq raw and analyzed data	This paper and *Lim, et al (2022)*[94]	GEO: GSE180294

(*Continued on next page*)

Continued

REAGENT or RESOURCE	SOURCE	IDENTIFIER
Experimental models: Cell lines		
Human: CS25iCTR18n6 (CTR18Q) iPSC line	Smith-Geater, et al (2020)[24]	N/A
Human: CS83iCTR33n1 (CTR33Q) iPSC line	*HD iPSC Consortium (2013)*[22]	N/A
Human: CS04iHD46n10 (HD46Q) iPSC line	*Smith-Geater, et al (2020)*[24]	N/A
Human: CS03iHD53n3 (HD53Q) iPSC line	*Smith-Geater, et al (2020)*[24]	N/A
Human: CS81iHD71n3 (HD71Q) iPSC line	*Lim, et al (2017)*[6]	N/A
Experimental models: Organisms/strains		
Mouse: R6/2: B6CBA-Tg(HDexon1)62Gpb/3J	The Jackson Laboratory	RRID: IMSR_JAX:006494
D. melanogaster: *HTT* repo: w; + ; HTT [231NT-128Q] - repo-gal4 / gal 80-TM6B	Laboratory of Dr. Juan Botas, *Onur et al (2021)*[42]	N/A
D. melanogaster: Control: Non-targeting hpRNA	Vienna Drosophila Resource Center	VDRC: 13974
D. melanogaster: *Nfl* KD: y[1]; Mi{y[+mDint2] = MIC}Nfl[MI06280]	Bloomington Drosophila Stock Center	RRID: BDSC_60792
D. melanogaster: *Nfl* glia KD: y[1] v[1]; P{y[+t7.7] v[+t1.8] = TRiP.JF02219}attP2	Bloomington Drosophila Stock Center	RRID: BDSC_31929
Software and algorithms		
Prism v9.4	GraphPad	RRID: SCR_002798
CellProfiler Image Analysis Software	CellProfiler	RRID: SCR_007358
ImageJ	ImageJ	RRID: SCR_003070
Imaris v9.9	BitPlane	RRID: SCR_007370
R v4.1.2	R Core Team	RRID: SCR_001905
Cell Ranger v3.1.0	10x Genomics	RRID: SCR_017344
Seurat v3.1	Satija Lab	RRID: SCR_016341
Ingenuity Pathway Analysis (IPA)	QIAGEN	RRID: SCR_008653
Enrichr	Ma'ayan Laboratory	RRID: SCR_001575
Empiria Studio v1.3.0.83	LICOR	RRID: SCR_022512
Other		
Matrigel™ hESC-Qualified Matrix	Corning	Cat#354277
mTeSR™1 Complete Kit	STEMCELL Technologies	Cat#85850
PSC Neural Induction Medium	Life Technologies	Cat#A1647801
DMEM, high glucose, pyruvate	Life Technologies	Cat#11995–065
Fetal Bovine Serum, certified, heat inactivated	Life Technologies	Cat#10082–147
GlutaMAX™ Supplement	Life Technologies	Cat#35050061
N-2 Supplement (100X)	Life Technologies	Cat#17502048
BrainPhys™ Neuronal Medium	STEMCELL Technologies	Cat#05790
NeuroCult™ SM1 Neuronal Culture Supplement	STEMCELL Technologies	Cat#05711
Neurobasal™ Medium	Life Technologies	Cat#21103–049
Sodium Pyruvate (100mM)	Life Technologies	Cat#11360070
SATO Supplement (100X)	*Chen, et al (2008)*[88]	N/A
Revert™ 700 Total Protein Stain for Western Blot Normalization	LI-COR Biosciences	Cat#926-11011

RESOURCE AVAILABILITY

Lead contact

Further information and requests for resources and reagents should be directed to and will be fulfilled by the lead contact, Leslie M. Thompson (lmthomps@uci.edu).

Materials availability

This study did not generate new unique reagents.

Data and code availability

- Data used in statistical analyses have been deposited in the paper's supplemental information and are available as of the date of publication.
- The single-nucleus RNA-seq data that supports the findings of this study have been deposited in Gene Expression Omnibus (GEO) repository and are publicly available as of the date of publication. Accession numbers are listed in the key resources table.
- Any additional information required to reanalyze the data reported in this paper is available from the lead contact upon request.

EXPERIMENTAL MODEL AND SUBJECT DETAILS

iPSC lines and cell culture

HD and unaffected control iPSCs were generated via non-integrating episomal reprogramming of patient-derived fibroblasts (see Table S1).[6,22–24] The iPSC lines were characterized by morphological analysis and immunocytochemistry (see Table S3) for presence of pluripotency markers and lack of differentiation markers. All iPSC lines exhibited normal karyotypes by aCGH array performed by Cell Line Genetics (Madison, WI). The five iPSC lines were maintained on Matrigel hESC-qualified matrix (Corning) with mTeSR1 (STEM CELL Technologies). Once 60–80% confluent, iPSCs were passaged using a 5–10 minute incubation with Versene (Gibco) at 37°C for expansion purposes.

Astrocyte differentiation

Five iPSC lines were differentiated into neural progenitor cells (NPCs) according to manufacturer's instructions (Gibco #A1647801, MAN0008031). NPCs were cultured to 90–95% confluency, then seeded at 1e5/cm^2 on hESC-qualified matrigel (Corning) for four passages before induction of astrocyte differentiation. All NPC lines exhibited normal karyotypes by aCGH array performed by Cell Line Genetics (Madison, WI) and expressed NPC/NSC markers as assessed by immunocytochemistry. To begin astrocyte differentiation, passage four NPCs were seeded at 7.5e4 cells/cm2 in Neural Expansion Medium (Gibco #A1647801) and the following day (day 0), half the medium was replaced with astrocyte differentiation medium (ADM) 1. Half media changes were performed every other day for the remainder of the differentiation. All subsequent passages were performed by washing cells with HBSS without Mg Ca (Gibco) three times, then incubating in StemPro Accutase (Gibco) at 37°C for 10–15 minutes, counting using TC20 Automated Cell Counter (Bio-Rad) with trypan blue exclusion, and seeding on hESC-qualified matrigel (Corning) at 5e4 cells/cm^2 unless otherwise noted. On day 7, the cells were replated in ADM1. On day 15, the cells were replated in 50% ADM1, 50% ADM2. Subsequent half media changes were performed using ADM2. On day 30, day 34, and day 45, the cells were seeded in 100% ADM3 at 4e4 cells/cm^2.[88] On day 60, the cells were subject to astrocyte enrichment via FACS. Quality control immunocytochemistry was performed at each passage time point for PSC, NPC, neural, and astrocytic markers. See Tables S2 and S3.

R6/2 mouse model

All experimental procedures were in accordance with the Guide for the Care and Use of Laboratory Animals of the NIH and animal protocols were approved by Institutional Animal Care and Use Committees at the University of California Irvine (UCI), an AAALAC accredited institution. For this study, five-week-old R6/2[31] and non-transgenic (NT) male mice were purchased from Jackson Laboratories and housed in groups of up to five animals/cage under a 12-hour light/dark cycle with *ad libitum* access to chow and water. Mice were aged to 8, 10, or 12 weeks then euthanized by pentobarbital overdose and perfused with 0.01 M PBS. Striatum and cerebral cortex were dissected out of each hemisphere and flash-frozen for snRNA-seq (8 and 12 weeks) or immunohistochemistry (10 weeks).

Fly husbandry

Fly lines were generated as described[89] or ordered from the Bloomington *Drosophila* Stock Center (BDSC) or Vienna *Drosophila* Stock Center (VDSC). A 231 amino acid N-terminal fragment of *mHTT* with 128 glutamines was expressed using a pan-glial (*repo*) driver. This line was generated in the Botas lab at Baylor

College of Medicine and kindly provided as a gift. Flies were maintained at 18°C or 23°C on standard fly food (molasses, yeast extract, and agar).

METHOD DETAILS

FACS astrocyte-enrichment

Day 60 iAstros were washed with HBSS without Mg Ca (Gibco) three times then lifted using a 10–15 minute incubation of StemPro Accutase (Gibco) at 37°C. Cells were collected and strained through a 70 μm cell strainer then incubated with 100U/mL DNaseI (Qiagen) in FACS Buffer (0.5% BSA [Gibco] in PBS without Mg and Ca) for 10 minutes at room temperature. Cells were washed, collected, then stained for GLAST-APC (Miltenyi Biotec; see Table S3) in FACS Buffer for 15 minutes at 4°C in the dark. Cells were washed, 40 μm strained, then collected, then stained for DAPI in FACS Buffer for 5 minutes at room temperature in the dark. Cells were immediately sorted on the FACSAria Fusion Cell Sorter (BD Biosciences) into ADM3 with PenStrep (Gibco). GLAST-positive/DAPI-negative cells were replated on hESC-qualified matrigel at a seeding density of 4e4 cells/cm^2 (0.38e6 cells/well of a 6-well) in ADM3 with 1x PenStrep. Following astrocyte-enrichment, the cells were cultured for another 7 days before harvest with half media changes every other day in ADM3 with 1x PenStrep followed by immunocytochemistry quality control analysis for astrocyte markers.

Immunocytochemistry

Cells were fixed using 4% paraformaldehyde (Electron Microscopy Sciences) in PBS for 10 minutes at room temperature. Depending on antigen, cells were permeabilized with 0.3% Triton X-100 (Sigma-Aldrich) in PBS for 10 minutes at room temperature. Cells were blocked for 1 hour in 10% goat serum (Gibco), 1% BSA (Gibco), 0.1% Triton X-100 in PBS for 1 hour at room temperature. Cells were incubated with primary antibodies (see Table S3) overnight at 4°C and then washed three times with PBS before incubation in 1:1000 Alexa-Fluor 488, 594, 647 secondary antibodies (Invitrogen) for 1 hour at room temperature and subsequently incubated with Hoechst 33342 (Sigma-Aldrich) for 10 minutes at room temperature. Stained slides were mounted with Fluoromount-G (Southern Biotech). Cells were imaged with a Nikon T-E fluorescence microscope at 10x and 20x. Analysis of images were performed by Cell Profiler[90] or ImageJ (FIJI).

Sholl and morphometric analysis

Individual iAstros (CTL and HD lines, n = 25–40 cells per replicate, 5 differentiation replicates per genotype) were imaged on a Fluoview FV3000 Olympus Confocal Microscope at 40× magnification. iAstros were analyzed by Simple Neurite Tracer (SNT) in ImageJ,[91] which provides 2D visualization of z-stack images. Images were z-projected to max intensity, changed to grayscale, and inverted for easier visualization. The SNT plug-in was accessed through Neuroanatomy, Deprecated, and then Simple Neurite Tracer. To build a primary path, a point was placed at the base of the path and then connected to the end of the path. Daughter paths were extended from these parent paths and to outline the full morphology. The primary and secondary number and path length were collected. Additionally, based on the paths, Sholl[92] was conducted to assess the complexity of each iAstros calculated by the number of intersections and concentric circles at 1 μm sequentially distant radii.[92,93]

Glutamate uptake assay

Glutamate uptake from iAstros was detected using an enzymatic, colorimetric glutamate assay kit (Abcam, ab83389). Day 67 GLAST-positive astrocytes were thawed and seeded into an hESC-qualified matrigel coated 96-well plate at 4e4 cells/cm^2. After 48 hours (day 69), iAstros were incubated with HBSS without Ca^{2+} and Mg^{2+} (without phenol red) for 30 minutes and then incubated with 200 μM L-glutamic acid for 120 minutes at 37°C. Cells were collected, counted, and processed according to manufacturer's instructions.

F-actin in-cell western

Day 67 GLAST-positive astrocytes were thawed and seeded into an hESC-qualified matrigel coated 96-well plate at 4e4 cells/cm^2 for 3 technical replicates per biological (differentiation) replicate per cell line. Two days post seeding, cells were fixed using 4% paraformaldehyde (Electron Microscopy Sciences) in PBS for 20 minutes at room temperature. After washing cells three times with 0.1% Tween 20 (Sigma-Aldrich) in PBS, cells were permeabilized with 0.2% Triton X-100 (Sigma-Aldrich) in PBS for 30 minutes at room temperature. Cells were then blocked for 1 hour in 5% goat serum (Gibco), 3% BSA (Gibco) in PBS for 1 hour at

room temperature. Cells were incubated with Phalloidin-iFluor790 (Abcam, ab176763) at 1:1000 for 1 hour at room temperature, followed by washing three times with 0.1% Tween 20 (Sigma-Aldrich) in PBS. CellTag700 (LI-COR, 926–41090) at 1:500 was added as a total protein stain (for normalization purposes) and incubated for 1 hour at room temperature. Cells were then washed three times with 0.1% Tween 20 (Sigma-Aldrich) in PBS, then solution was completely removed from wells. Wells were immediately imaged using the LI-COR Odyssey CLx and analyzed using LI-COR's Empiria Studio Software.

Western blots

Day 67 GLAST-positive astrocytes were broken in 150uL modified RIPA buffer, sonicated three times for 10 seconds at 40%, then spun down for 20 minutes at 4°C, 1000 rpm. Bradford (Thermo Scientific BioMate 3S UV-visible spectrophotometer) protein quantification was performed with cuvettes. Protein lysates were aliquoted at 5 μg for GluR1, ACTN, ATF3, and SOX9 (see Table S3). Then equivalent amounts of loading buffer were added. Gels were run at 150 V using Bolt™ 4–12% Bis-Tris Plus Gels, 15-well gels with MOPS, transferred onto Nitrocellulose Membrane 0.45 μm at 10 V for 1 hour at room temperature. The membrane was rinsed in water and then let dry for 15 minutes. Membranes were rehydrated in water and then followed the Revert 700 Total Protein Stain protocol. Membranes were blocked in Intercept (TBS) Blocking Buffer for 1 hour at room temperature. Membranes were incubated in primary antibody (GluR1, ACTN, ATF3, and SOX9) and rotated at 4° overnight. Membranes were then washed three times with TBST, then incubated in secondary antibody: GluR1 into IRDye® 800CW Goat anti-Rabbit IgG, ACTN into IRDye® 800CW Goat anti-Mouse IgG, ATF3 into IRDye® 800CW Goat anti-Mouse IgG, and SOX9 in IRDye® 700CW Goat anti-Rabbit IgG for 1 hour at room temperature. Membranes were washed three times with TBST while gently shaking for 1 hour, then washed two times with TBS at room temperature. Membranes were imaged using the LI-COR Odyssey CLx and analyzed using LI-COR's Empiria Studio Software.

Single-nuclei RNA-sequencing

Mouse

Single nuclei from three mice per genotype per timepoint were isolated from half hemisphere striatum or cortex in Nuclei EZ Lysis buffer (Sigma-Aldrich, NUC101-1KT) and incubated for 5 minutes. Samples were passed through a 70 μm filter and incubated in additional lysis buffer for 5 minutes and centrifuged at 500 rcf for 5 minutes at 4°C before two washes in Nuclei Wash and Resuspension buffer (1x PBS, 1% BSA, 0.2 U/μL RNase inhibitor). Nuclei were FACS sorted using DAPI to further isolate single nuclei and remove additional cellular debris. These nuclei were run on the 10x Genomics® Chromium Single cell 3' gene expression v3 platform. Libraries were quality controlled and sequenced on the Illumina NovaSeq 6000.

iAstros

Day 67 GLAST-positive cells were thawed and seeded into hESC-qualified matrigel coated 6-well plates at 4e4 cells/cm^2 in ADM3 (see astrocyte differentiation). After 48 hours, day 69 GLAST-positive cells were washed with HBSS without Mg Ca (Gibco) three times then lifted using a 10–15 minutes incubation of StemPro Accutase (Gibco) at 37°C. Single-cell suspensions were strained using a 70 μm strainer, washed using cold 0.08% BSA (Gibco) in PBS, and counted using TC20 Automated Cell Counter (BioRad) with trypan blue exclusion per manufacturer's instructions in the 10x Genomics® Demonstrated Protocol: Single Cell Suspensions from Cultured Cell Lines for Single Cell RNA Sequencing (Document CG00054). To obtain a single-nuclei suspension, cells were lysed using Nuclei EZ Lysis Buffer (Sigma Aldrich, NUC101-1KT) for 5 minutes on ice. Lysed cells were centrifuged 500 rcf for 5 minutes at 4°C, then washed by twice resuspending in 1% BSA (Gibco), 0.2 U/μL of Human Placenta RNase Inhibitor (NEB), in PBS and centrifuged again. After two washes, the nuclei were strained using a 40 μm cell strainer, counted using the TC20 Automated Cell counter (Bio-Rad), resuspended at 1000 nuclei/μL in 0.08% BSA (Gibco) in PBS, then proceeded immediately with the 10x Genomics® Chromium Single cell 3' gene expression v3 platform. Libraries were quality controlled and sequenced on the Illumina NovaSeq 6000.

Data processing

Mouse

A total of 109,053 cells with 6.1 billion reads were sequenced for the 24 samples (on average 4,544 cells per sample with ~56K reads per cell). Alignment was done using the CellRanger pipeline v3.1.0 (10x Genomics) to a custom pre-mRNA transcriptome built from refdata-cellranger-mm10–1.2.0 transcriptome using

cellRanger mkref. To filter out low-quality nuclei and low-abundance genes, nuclei with less than 200 genes or more than 6000 genes and percent mitochondrial reads aligning to more than 2% of mitochondria genes were excluded from the downstream analyses. UMI counts were then normalized in Seurat 3.0 and top 2000 highly variable genes were identified using FindVariableFeatures function with variance stabilization transformation (VST). UMI Count matrices were generated from BAM files using default parameters of cellRanger count command. The gene barcode matrices for each sample were imported into R using the Read10X function in the Seurat R package[94] v3.1.5. Replicates were combined using cellRanger aggr. Dimension reduction was used to visualize and explore major features of the data using PCA and UMAP. Clustering was performed in Seurat v3.1 using PC1-20 and 0.5 resolution. The cluster with highest expression of astrocyte markers (Slc1a2, Slc1a3, Aldh1l1, S100β) were computationally subset to isolate a single astrocyte cluster for each dataset. Subclustering of astrocyte clusters was performed using PC1-20 and the following resolutions: 0.5 for striatal and cortical 12-week, 0.3 for striatal 8-week, and 0.5 for cortical 8-week.

iAstros

A total of 37,170 cells with 2.3 billion reads were sequenced for the 4 samples (on average 9,293 cells per sample with ~61K reads per cell). Fastq files were quality controlled and aligned to the GRCh38 reference transcriptome to obtain a gene count matrix using Cell Ranger pipeline v3.1.0 (10x Genomics). To filter out low-quality nuclei and low-abundance genes, nuclei with less than 200 genes or more than 6000 genes and percent mitochondrial reads aligning to more than 5% of mitochondria genes were excluded from the downstream analyses. UMI counts were then normalized in Seurat R package[94] v3.1.5 and top 2000 highly variable genes were identified using FindVariableFeatures function with variance stabilization transformation (VST). After quality control and expression matrix formation, normalization was performed using UMI, and log-transformation was used to control variance. Seurat integration was used to combine datasets from patient-derived cell lines. Dimension reduction was used to visualize and explore major features of the data using PCA and UMAP. Clustering was performed in Seurat v3.1 using PC1-20 and 0.2 resolution.

Differential gene expression and pathway analysis

To identify gene expression differences between clusters and/or samples, a non-parametric Wilcoxon rank sum test was used with Bonferroni correction and 1% FDR cutoff using Seurat v3.1 (see Data S1 and S2). Cell types were assigned to clusters based on known cell-type markers. Data will be deposited in GEO. QIAGEN's Ingenuity Pathway Analysis (http://www.qiagen.com/ingenuity) and Enrichr (https://maayanlab.cloud/Enrichr/)[36,37] were used for analysis of significantly differentially expressed genes (FDR<0.1).

Immunohistochemistry and confocal microscopy

Three male mice per genotype at 10 weeks of age were euthanized by pentobarbital overdose and perfused with 0.01 M PBS. Whole brains were drop-fixed in 4% paraformaldehyde (Electron Microscopy Sciences) in PBS overnight at 4°C, then 30% sucrose for 48 hours at 4°C. Half brain was embedded in Tissue-Tek O.C.T. Compound (Fisher Scientific) and sectioned coronally at a section thickness of 14 μm on a cryostat at −20°C. Tissue was collected as free-floating sections in PBS with 0.05% sodium azide stored at 4°C. For staining, antigen retrieval with sodium citrate buffer (10mM Sodium Citrate, 0.05% Tween 20, pH 6.0) at 80℃ for 30 minutes was performed with floating tissue sections. The sections were permeabilized for 15 minutes in 1x PBS, 0.25% Triton X-100, and 3% BSA (Gibco), and then blocked in 1x PBS, 0.1% Triton X-100, 10% Donkey Serum (Gibco) and 1% BSA. Sections were then immediately placed in a primary antibody (see Table S3) diluted mix in 1x PBS, 5% Donkey Serum, and 0.1% TritonX-100 overnight at 4°C. Sections were washed three times with 1x PBS before incubation in 1:500 Alexa-Fluor 488, 594, 647 secondary antibodies (Invitrogen) for 1 hour at room temperature and subsequently incubated with Hoechst 33342 (Sigma-Aldrich) for 10 minutes at room temperature. Sections were mounted on microscope slides, coverslipped with Fluoromount-G (Southern Biotech), and visualized and captured using a Fluoview FV3000 Olympus Confocal Microscope at 60x magnification. For the analysis, three tissue sections encompassing the majority of the striatum (dorsolateral, medial, and inferior regions) were imaged per mouse for a total of 16 images per mouse. (n = 3 male mice/genotype, 3 sections/mouse, 2–3 regions/section, 2 images/region). Imaris Cell Imaging analysis software v9.9 (Bitplane) was used to analyze SOX9 intensity (maximum and mean) number of DAPI and number of SOX9 positive cells using the Surfaces mode. SOX9 intensity was averaged based on the number of SOX9 positive cells that were in the image frame.

Fly climbing assay

Virgin female flies harboring the *mHTT* transgene or control flies (VDSC 13974) were crossed to males harboring experimental alleles. Experimental crosses were raised and maintained at 25°C. Only female progeny were assessed using the climbing assay. Anesthetized using carbon dioxide, female progeny were sorted into vials used for experimentation without food in groups of 9 to 10 flies with 10 replicates (biological replicates). The percent of flies that climbed to or past 5 cm in 10 seconds at room temperature were quantified. Tapping was used to elicit negative geotaxis to force flies to the bottom of the vials with 3 rapid succession taps, three times, over 2 seconds. Flies were allowed to climb for 10 seconds, and a picture was taken against a white background with a mark parallel to the lab bench at 5 cm from the bottom of the vial. After a 1-minute recovery, the 10 second climbing trial was repeated for a total of five times (technical replicates). Flies were climbed at days 7 and 10 post-eclosion.

QUANTIFICATION AND STATISTICAL ANALYSIS

All features highlighted in the paper and reported as statistically significant have p-values < 0.05 or adjusted p-values (FDR) < 0.1, unless otherwise stated.